

Natural Night Sky Brightness during Solar Minimum

MIGUEL R. ALARCON ^{1,2} MIQUEL SERRA-RICART ^{1,2} SAMUEL LEMES-PERERA ¹ AND MANUEL MALLORQUÍN ^{1,2,3}

¹*Instituto de Astrofísica de Canarias, C/Vía Láctea s/n, E-38205 La Laguna, Canarias, Spain*

²*Departamento de Astrofísica, Universidad de La Laguna, E-38205 La Laguna, Canarias, Spain*

³*Sieltec Canarias S.L., C/ Habitat, No. 2, Portal D, Of. 3, E-38204 La Laguna, Canarias, Spain*

(Received April 5, 2021; Revised April 22, 2021; Accepted April 29, 2021; Published June 22, 2021)

ABSTRACT

In 2018, Solar Cycle 24 entered into a solar minimum phase. During this period, 11 million zenithal night sky brightness (NSB) data were collected at different dark sites around the planet, including astronomical observatories and natural protected areas, with identical broadband Telescope Encoder and Sky Sensor photometers (based on the Unihedron Sky Quality Meter TSL237 sensor). A detailed observational review of the multiple effects that contribute to the NSB measurement has been conducted with optimal filters designed to avoid brightening effects by the Sun, the Moon, clouds, and other astronomical sources (the Galaxy and zodiacal light). The natural NSB has been calculated from the percentiles for 44 different photometers by applying these new filters. The pristine night sky was measured to change with an amplitude of 0.1 mag/arcsec² in all the photometers, which is suggested to be due to NSB variations on scales of up to months and to be compatible with semiannual oscillations. We report the systematic observation of short-time variations in NSB on the vast majority of the nights and find these to be related to airglow events forming above the mesosphere.

Keywords: Atmospheric effects (113); Night sky brightness (1112); Astronomical instrumentation (799); Photometer (2030); Astronomical site protection (94); Observational astronomy (1145); Astronomy data analysis (1858)

1. INTRODUCTION

The natural night sky is never completely dark. Even in the most isolated places, there is a background skyglow resulting from both a natural component of terrestrial and extraterrestrial origin and an artificial skyglow component resulting from human activity. Artificial skyglow is the brightening of the night sky due to the scattering of artificial light at night (ALAN) by the constituents of the atmosphere (mainly gas molecules, aerosols, and clouds) in the direction of observation. It includes radiation that is emitted directly from the ground and reflected upward from the surface. The loss of darkness due to the increasing use of ALAN has a dangerous, but sometimes neglected, impact on natural ecosystems (Hölker et al. 2010; Gaston et al. 2013; Bennie et al. 2016; Owens & Lewis 2018). Estimates

suggest that more than one-tenth of the planet's land area experiences ALAN and that figure rises to 23% if atmospheric skyglow is included (Falchi et al. 2016). Indeed, artificially lit outdoor areas brightened at a rate of 2.2% per year between 2012 and 2016 (Kyba et al. 2017).

ALAN emissions from cities have been monitored using instruments on Earth-orbiting satellites (de Miguel et al. 2020). However, evaluating the effects of these emissions on night sky brightness (NSB) in dark places (normally natural protected areas or astronomical observatories) requires extensive groundbased observations. NSB as seen from the ground is generated by several sources (see Roach & Gordon (1973) and Leinert et al. (1998) for an exhaustive overview). When the Moon is above the horizon, its scattered light is the brightest component of the entire night sky. On dark nights and in less polluted places, the combination of starlight and diffuse Galactic light (DGL) is also significant, followed by the scattering effect of sunlight on interplanetary dust that leads to faint zodiacal light lying around

the ecliptic plane. While the stationary contribution of these sources is linked to their reference planes, the chemiluminescent emission of molecules above the mesosphere, known as airglow, is not. This is not only one of the most relevant components of the NSB in dark skies but also a determining factor in its variability, which depends on several parameters (season, geographical position, solar cycle, and so on) interacting in a largely unpredictable way. Several studies have been made to characterize night sky brightness and its variability at the main telescope sites (Walker 1988; Leinert et al. 1995; Mattila et al. 1996; Krisciunas 1997; Benn & Ellison 1998; Patat 2003, 2008). However, a regular and systematic study is necessary to monitor possible trends toward the brightening of the global natural NSB and to investigate the different processes driving its variability.

The analysis presented here is based on zenith NSB measurements performed by a night photometer network deployed by the European project STARS4ALL (Zamorano et al. 2017a). Zenithal NSB, despite having considerably limited information content than all-sky or photometric systems, is widely used to characterize NSB. This is partly due to the widespread availability of low-cost detectors that enable its straightforward measurement by professional and citizen scientists worldwide (Sánchez de Miguel et al. 2017; Posch et al. 2018; Puschnig et al. 2020). This work aims to define the first comprehensive reference method to combine measurements from several low-cost broadband photometers distributed in different locations for the study of natural night sky darkness. This will allow us first to determine the intensity of the local skyglow and then to study its variability and possible origin by detecting the changes that the artificial disruption of night sky darkness may experience in the coming years. This is a relevant issue not only for preservation of the capabilities of observational astronomical sites Walker (1970) but also for biodiversity preservation, urban emission monitoring (Bustamante-Calabria et al. 2021), energy economics (Gallaway 2010), and preservation of the night sky as a key asset of the intangible cultural heritage of humanity.

The paper is organized as follows. The different detectors used in data acquisition are described in Section 2; the method of filtering data with different constraints (e.g., clouds, the Moon, and Galactic and zodiacal light) is discussed in Section 3, and the results obtained during dark time are then presented in Section 4. Timescale variations and their origin are analyzed in Section 5 and the main conclusions are presented in Section 6. Finally, detailed discussions about the photometric, calibration,

and instrumental uncertainties of the Telescope Encoder and Sky Sensor (TESS) photometer are given in the Appendix.

2. DATA ACQUISITION

2.1. TESS Photometer and Sky Quality Meter

The European-funded project STARS4ALL¹ has recently developed a new detector that uses the same TSL237 photodiode detector as the Sky Quality Meter (SQM; Cinzano (2007)). It is a silicon photodiode with a light-to-frequency converter, which has a spectral response that varies from 300 to 1100 nm approximately, with a sensitivity maximum around 700 nm, responding linearly to frequency over several irradiance orders (Bará et al. 2019). This instrument is called TESS Zamorano et al. (2017a)). The SQM uses a Hoya CM-500 filter for nominally limiting its effective bandpass to 400–650 nm, whereas TESS is fitted with a dichroic filter that limits it to the 400–740 nm spectral band, allowing for better coverage of the red band of the visible spectrum with good response (the spectral response of these photometers is shown in the Appendix). A concentrator optic restricts the device field of view (FOV) to a region of the sky with an approximately Gaussian transmittance profile with an FWHM of 17°.

TESS was designed with the goal of creating a large European network with inexpensive but well-tested photometers. In fact, the device is calibrated by the manufacturer at the Laboratory for Scientific Advanced Instrumentation (Laboratorio de Instrumentación Científica Avanzada) of Universidad Complutense de Madrid (UCM, Spain) and contains a complete system to transmit data to STARS4ALL servers. At present more than 200 photometers are installed and sending data worldwide, which are available at the project website². To avoid mistakes, it is necessary to consider the TESS and SQM responses as those of different photometric systems. The conversion factors between TESS, the SQM, and other photometric systems can be obtained based on the kind of spectrum of the observed object (Bará et al. 2019). Hereafter the brightness in magnitude per square arcsecond measured in the TESS and SQM passbands will be called m_{TESS} and m_{SQM} , respectively. A total of 44 TESS photometers (see Table 2) and 11 million individual raw measurements have been included in the present work. A detailed analysis of the uncertainties existing in the pho-

¹ www.stars4all.eu

² tess.dashboards.stars4all.eu

tometer data and the differential photometry is given in the Appendix.

2.2. *ASTMON all-sky camera*

The All-sky Transmission Monitor (ASTMON) instrument is designed to perform continuous monitoring of NSB in several bands (Aceituno et al. 2011). At present two ASTMON stations are installed at Observatorio del Roque de los Muchachos (ORM, La Palma) and a third one at Observatorio del Teide (OT, Tenerife) in the Canary Islands, all operated by Instituto de Astrofísica de Canarias (IAC, Spain). All are fully robotic and have standard Johnson–Cousins *BVRI* filters (Bessell 1990).

2.3. *Light pollution laboratory*

The measurements gathered by the STARS4ALL network are openly available in real time for researchers and the public at the Internet of Things EELabs (IOT-EELab) website³. IOT-EELab is an interactive website dashboard that collects, controls, and analyzes data from hundreds of internetconnected light pollution devices, including night photometers, LED control sensors, and all-sky cameras. IOT-EELab provides a unique opportunity for researchers to experiment with new and existing light pollution data sets to apply data science and big data techniques to gain new insights and valuable information, or build their own applications or research projects.

3. DATA ANALYSIS

NSB as seen from the ground is generated by several layers at vastly different distances. Neglecting the small contribution from extragalactic background light (which, at visible wavelengths, represents only 0.2% of the total NSB; see Table 4 of Masana et al. (2021)), the main contributors to NSB are integrated starlight (ISL) and diffuse background radiation (both originating in our Galaxy); zodiacal light, caused by the scattering of solar radiation from interplanetary dust; airglow emission from high atmospheric layers; and the scattering of these components in the troposphere (Leinert et al. 1998). In addition to these natural components, human activity has added an extra source, namely the artificial light emitted upward from cities and scattered back by the troposphere. New analytical techniques that select those data points that are uninfluenced by the Sun, the Moon, clouds, and astronomical sources (Galactic and zodiacal light) are presented in the following sections.

3.1. *Cloud coverage analysis*

One of the main natural factors that affect sky brightness measurements is the presence of clouds in the photometer’s FOV. When illuminated by either natural (the Moon) or artificial (ALAN) external sources, clouds produce a significant increase in the skyglow of urban sites (Kyba et al. 2011; Jechow et al. 2017), whereas the opposite occurs in dark areas (Jechow et al. 2019). Therefore, defining a robust method so it has only cloudless nights and knowing the uncertainty associated with them is essential in order to properly characterize the NSB. In this work, the performance of two different methods is tested: one based on the difference between the ambient and IR temperatures of the sky, obtained with the thermometers incorporated in TESS, and another based on the high variability in the measurement of NSB in the presence of clouds given by the standard deviation (Cavazzani et al. 2020).

While in the former method measurements of NSB and the ambient and IR temperatures are taken simultaneously, in the latter it is mandatory to define a period just before the reading over which the standard deviation is calculated. Choosing the length of the period is not trivial, as the σ_{TESS} distribution tends to spread out as it gets longer –see Figure 1. This is a consequence of the many factors involved in the short-term variability of sky brightness that are analyzed in this work. Both the value of σ_{TESS} and the length of the period must be fine-tuned to filter out the cloudy data.

To test the performance of both methods, ~ 4000 all-sky images taken with All-sky Meteor Orbit System (AMOS) cameras (Zigo et al. 2013) at OT and ORM during 2019 have been labeled visually. These high-sensitivity cameras designed for meteor detection make the presence of thin cirrus clouds distinguishable in the FOV covered by TESS. There is a bias of more meteors detected on clear nights, which represent three quarters of the whole data set. To balance out this proportion, overcast nights are added. At OT there are two cloud (Song and Open University Telescopes) and four humidity detectors (Song, Open University, STELLA Telescopes, and Residence). The sky is considered completely overcast when both cloud detectors are positive and humidity is 100% in all four detectors. For each method and period, the measurements of the photometers stars211 (OT) and stars90 (ORM) are merged with the AMOS images and inspected. Cloudlessness is deemed to occur when all the images within the period have been classified as clear, conditions otherwise being considered cloudy. In total, between 33,000 (for a period of 40 minutes) and 15,000 (10 minutes) TESS measure-

³ data.eelabs.eu

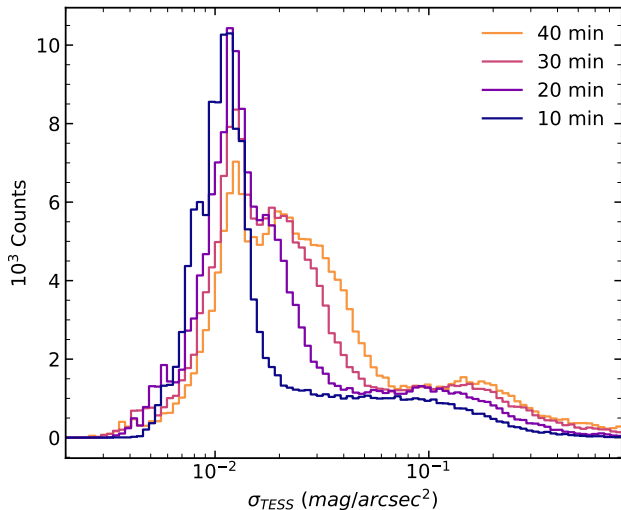


Figure 1. Standard deviation σ_{TESS} of NSB calculated over different time periods. Each distribution has $\sim 200,000$ data, measured with the photometer stars211 located at the Observatorio del Teide (Tenerife, Canary Islands, Spain). Data affected by the Sun and Moon have been filtered out.

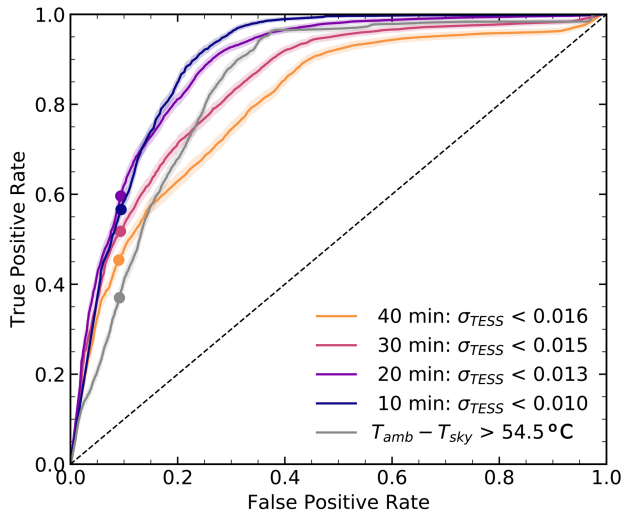


Figure 2. ROC curves for the standard deviation method σ_{TESS} , calculated for different periods, and the temperature difference method (black). The dots indicate the points where the criterion $\text{FPR} = 0.1$ is satisfied, whose threshold for the data to be considered cloudless is indicated in the legend. The diagonal dashed line is the reference for a random classifier.

ments unaffected by sunlight and moonlight have been annotated as clear/cloudy and used to test the methods.

To fine-tune the threshold to below where the sky is considered cloudless, the receiver operating charac-

teristic (ROC) curve Swets (1988)) has been obtained for both methods. It represents the true-positive rate (TPR) against the false-positive rate (FPR) for a range of threshold values, and can be used to compare different models, as shown in Figure 2. A classifier is considered to be good when it maximizes the TPR, losing less clear data, while minimizing the FPR, reducing the probability of including partially/totally cloudy data as clear. To avoid possible deviations due to different data set sizes and to estimate the uncertainty in the TPR and FPR, the data set has been bootstrapped by taking 1000 random samples of 5000 data with replacements and calculating their median and 95% confidence interval, which are shown in the figure as a thick line and band, respectively.

There is no universal criterion for choosing the threshold. Although the closest to the top left corner is usually taken as the best value, this may depend on the specific conditions of the problem. We are interested in filtering out data with some cloud presence as far as possible, even if this means losing a lot of clear data. The authors consider that an FPR of 10% is reasonable for the study of natural NSB with these low-cost photometers, but other equally valid values could be chosen for other types of studies, interests, or instruments. The points that meet this criterion are shown on the ROC curves and the threshold is included in the legend. It should be noted that the σ_{TESS} method with a period of 10 and 20 minutes is better than the temperature difference method—which is used by default in the TESS photometers—over the whole range. Both intervals are similar in the low-FPR region and even though for 20 minutes the FPR is a little bit higher than that for 10 minutes, the latter is considered to be the better one for our purposes. First, the shorter the period, the smaller, on average, the difference between the measurement and the labeled data timestamp being compared, thus increasing the reliability of the true-condition data set. On the other hand, the global performance of a classifier can be estimated by the area under the curve (AUC), considered better if it is closer to 1—closer to the upper left corner—or to 0.5 for a random choice (the diagonal dashed line in the figure). The highest AUC is obtained by taking a 10 minute interval, 0.892 ± 0.005 , followed by a 20 minute interval, 0.881 ± 0.006 , and the temperature difference, 0.837 ± 0.007 . Hence, cloudlessness is considered to occur when the standard deviation of the sky brightness measurements in the preceding 10 minutes is $\sigma_{\text{TESS}} < 0.010 \text{ mag/arcsec}^2$, with a TPR of 0.566 ± 0.015 and an FPR of 0.094 ± 0.006 .

At this point, it should be noted that these curves and thresholds may be different for brighter locations, as there is a dependency of the standard deviation on NSB, as noted by Cavazzani et al. (2020). Our analysis is considered valid for the range of magnitudes studied in this work. Other methods such as the IR temperature or sky brightness derivative method proposed by Sciezor (2020) have been tested without better results.

One of the greatest advantages of knowing the TPR and FPR is being able to estimate correctly the percentage of clear night time on every photometer. If this were calculated by means of the fraction of data that fulfills the condition of σ_{TESS} against the total, the result would be highly biased, because it would include $\sim 10\%$ of false positives and discard $\sim 43\%$ of true positives. To correct this bias we use the Rogan–Gladden estimator (Rogan & Gladden 1978):

$$P_{\text{corr}} = \frac{P - \text{FPR}}{\text{TPR} - \text{FPR}} \quad (1)$$

where P and P_{corr} are the percentages of clear time before and after correction. The result for each photometer used in this paper is included in Table 2. The uncertainties in these values are estimated from the bootstrapped TPR and FPR ranges.

3.2. Astronomical components

In the following sections, we will use the combined information from all the available photometers to characterize the effects of the different astronomical components affecting the natural NSB. To do this, it is essential to correct for differences in brightness measurements at the different sites. To find the offset for each photometer we have taken the median value of its natural NSB, $P50_{\text{TESS}}$, as a reference, calculated iteratively from the clear data remaining after applying all the filters that will be discussed below. By subtracting the P50 values of each photometer from its magnitude measurements, they can be treated as independent samples as long as they are uncorrelated—this will be discussed extensively in Section 5.2. Hence, the variations in NSB that will be discussed hereafter have been characterized from the mean of the $m_{\text{TESS}} - P50_{\text{TESS}}$ of all the photometers and their standard errors.

3.2.1. Sun

Once the Sun goes below the horizon and civil twilight begins, the sky brightness starts to decrease quickly. As the solar elevation decreases, the atmospheric layers directly illuminated by the Sun become higher and the blue part of the zenith spectrum becomes stronger as a

result of ozone absorption until it reaches its maximum at the end of nautical twilight (12° below the horizon). From that moment on, when many of the brightest stars are already visible, the sky spectrum and intensity profile begin to flatten out, becoming gradually redder and darker until the end of astronomical twilight, when the elevation of the Sun is -18° (Spitschan et al. 2016). The reverse process occurs at dawn. In this study, it is considered, as is usually done in observational astronomy, that the NSB measurements are not affected by direct sunlight when the Sun is below -18° (see, for example, Figures 3–7 in Patat et al. (2006)). Other indirect effects related to solar radiation will be described below.

3.2.2. Moonlight

The Moon is the major contributor to natural light pollution at night, especially in the bluest part of the spectrum, because of the efficiency of Rayleigh/Mie scattering increasing toward shorter wavelengths (Noll et al. 2012). NSB due to scattered moonlight depends on many factors. First, the intensity of light that enters our atmosphere after being reflected by the lunar surface is a function of its albedo and distance. The albedo depends primarily on the phase, but also on the solar selenographic longitude and wavelength. The variation of the distance to the Moon can affect the incident intensity in the atmosphere by 10% at maximum (Jones et al. 2013). In the atmosphere, moonlight is affected by Rayleigh and Mie scattering, which depend mainly on the transmission of the atmosphere for the airmass of the Moon and the target, their angular separation, and their wavelength.

The fact that all our measurements have been taken at the zenith makes the problem much easier, especially in the treatment of scattering. The intensity of moonlight can be parameterized according to its phase–illumination–and elevation. Thus, we will analyze how NSB changes according to these two parameters. As a reminder, the aim of this work is not to make an empirical model of the different components that affect NSB, but to establish filters that allow us to minimize them to study the natural NSB. Figure 3 shows the NSB difference as a function of the elevation and phase of the Moon for all the photometers, filtering data affected by sunlight. The brightness curves remain constant for Moon elevations below -5° , regardless of phase. Above this value, it is considered that the measurements could be polluted by moonlight and should be filtered out. It should be noted that the $m_{\text{TESS}} - P50_{\text{TESS}}$ difference when the Moon is below the horizon does not reach 0

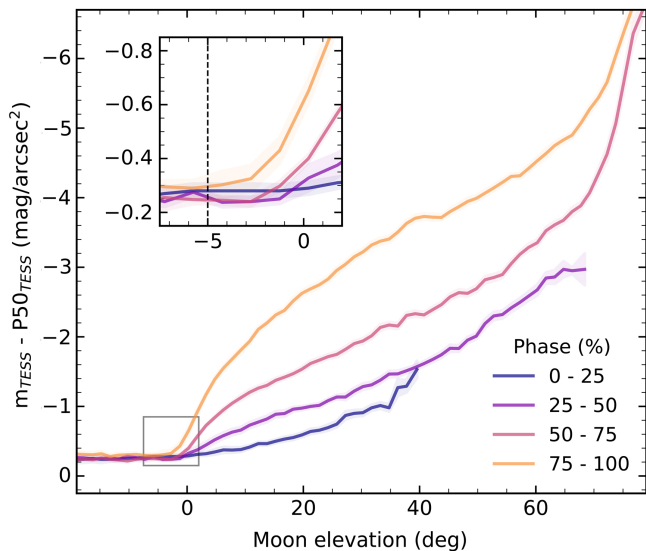


Figure 3. NSB difference against Moon elevation for different lunar phases. The region near the horizon is zoomed in on the inside plot, indicating the elevation (vertical dashed line) from which the data are filtered. All available photometers have been included, making a total of 8.13 million measurements.

because of the presence of other bright components such as the Galaxy and zodiacal light.

3.2.3. Galaxy

The Milky Way, zodiacal light, and airglow are the most important components affecting NSB on clear, moonless astronomical (Sun elevation $< -18^\circ$) nights in the visible spectral range. When observed very close to the Galactic plane, the contribution of starlight (ISL) and diffuse background radiation (DGL), which can be 20–30% of that integrated into the FOV of the photometer, may be the greatest of all (Leinert et al. 1998). This is especially the case at midlatitudes in the southern hemisphere, where the Galactic center is close to the zenith in fall and winter. Decoupling these three components in ground-based observations to study them separately is not trivial. The data taken by the imaging photopolarimeters on board Pioneer 10 and 11 during their journey beyond the outer asteroid belt are currently the main reference for determining the absolute brightness of the Galaxy (see, for example, Mellinger (2009), Zou et al. (2010), Noll et al. (2012)), because only in those regions of the solar system ($R > 2.8$ AU) is the contribution of zodiacal light negligible (Weinberg et al. 1974; Schuerman et al. 1977). Any other ground- or space-based ISL+DGL measurements must be either complemented by semiempirical models to correct for these contributions (e.g., Hoffmann et al. (1998); Duriscoe (2013); Gill et al. (2020)) or constrained to

specific observing conditions, which is the approach of this work.

To filter out the contribution of Galactic light, a visual inspection of the data from all the photometers, once sunlight, moonlight, and clouds have been filtered out, has been conducted and some common patterns have been identified. In the Galactic plane, the central region is clearly the brightest, with a rapid decrease toward the arms and smoother with increasing latitude. With such a wide FOV, inhomogeneities produced by dark clouds or star clusters in the Galactic plane are not expected to be detected, but high symmetry in both longitude and latitude is. It might be expected that, regardless of the Galactic longitude, the NSB difference due to the Galaxy would decrease at higher latitudes until it is almost residual. However, there are two regions where this does not apply: the center and the anticenter, where the Galactic and ecliptic planes are overlapped. Hence, a distinction has been made as to whether zodiacal light could be shifting the curves toward brighter values, according to the method discussed in Section 3.2.4.

The NSB difference as a function of the absolute value of the Galactic latitude for different longitudes is shown in Figure 4. In the region close to the Galactic center (blue line) the zenith sky brightness can increase by up to 1 mag/arcsec², while the average elsewhere in the Galactic plane reaches about 0.4 mag/arcsec². The effect of the ecliptic is also shown in the figure. While in the regions affected by zodiacal light the NSB difference does not reach 0 up to very high Galactic latitudes near the poles, the solid curves, corresponding to measurements far from the ecliptic, flatten out for $|b| \geq 40^\circ$. Therefore, in this work it will be considered that measurements are unaffected by Galactic light when the absolute value of the Galactic latitude at zenith is greater than 40° .

3.2.4. Zodiacal light

Zodiacal light is the result of the scattering of sunlight by interplanetary dust particles in the solar system. Its intensity depends mainly on ecliptic latitude β and helioecliptic longitude $\lambda - \lambda_\odot$, defined as the difference between the longitudes of the object, in our case the zenith, and the Sun. In contrast to the Galactic component, the brightness map of zodiacal light is not fixed to the celestial reference system, but depends on the position of the Sun in the sky and therefore on the location and time of year. As the Sun goes below the horizon and moves along the ecliptic, the brightness smoothly

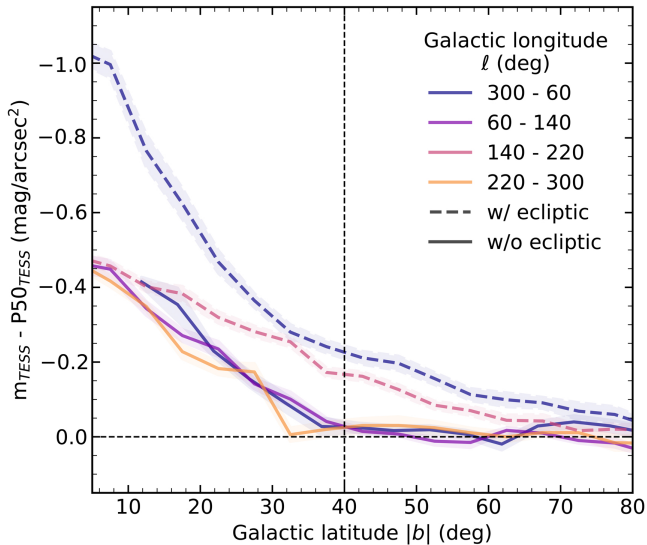


Figure 4. NSB difference against absolute Galactic latitude for different longitude intervals covering the center (blue), anticenter (pink), and arms (yellow and purple) of the Galaxy. Measurements that can be affected by zodiacal light according to Section 3.2.4 are shown as dashed lines, while the rest are shown as solid lines. To avoid the contribution of the Galaxy in the clean data, those with $|b| < 40^\circ$ are filtered out, indicated by a vertical black dashed line. All available photometers have been included, making a total of 1.44 million data on moonless and cloudless astronomical nights.

decreases until it reaches longitudes close to 180° , where it increases steeply in a small area of about 20° in diameter known as the Gegenschein (Leinert et al. 1998).

Several brightness maps have been used in the literature to take into account the contribution of zodiacal light. For instance, Patat (2003) interpolated the data presented by Levasseur-Regourd & Dumont (1980) to correct for zodiacal light in his observations from Cerro Paranal. An improved model made by Leinert et al. (1998) was used by Noll et al. (2012) and Masana et al. (2021) to account for reddening and thermal emission. Likewise, the model obtained by Kwon et al. (2004) from photopolarimetric data taken on consecutive nights from Mount Haleakala in Hawaii was used as a reference by Duriscoe (2013) and Gill et al. (2020) to quantify brightness excess due to zodiacal light. Right from the outset of this work, we have avoided doing any model-derived correction in order to directly process the raw data.

After filtering out the effect of the Sun, Moon, clouds, and Galaxy, there are still 520,000 data left with which to study the contribution of zodiacal light. To avoid possible post-twilight brightness enhancements, which are

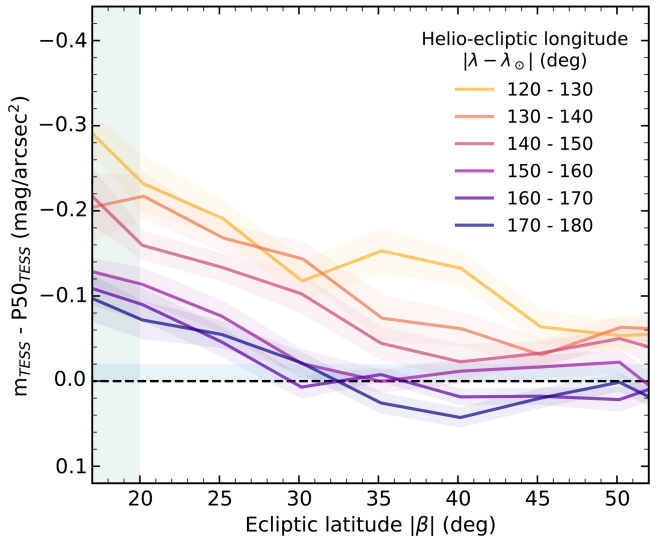
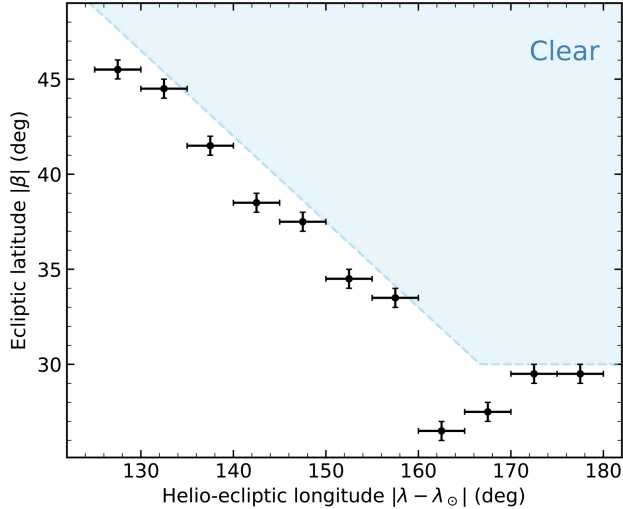


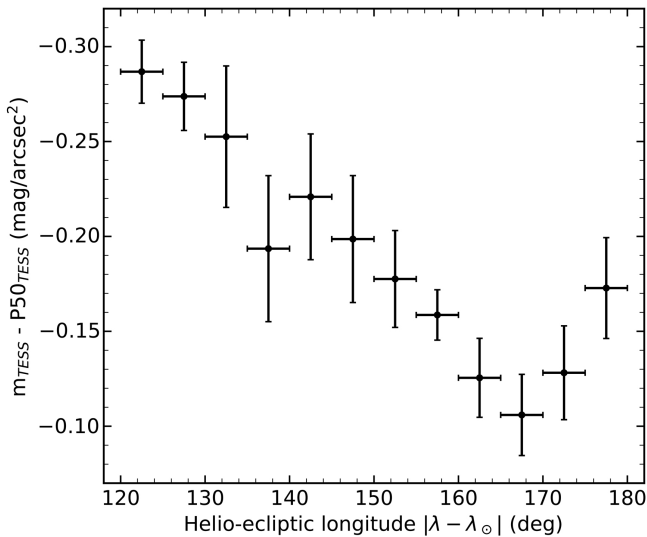
Figure 5. NSB difference against absolute ecliptic latitude for different helioecliptic longitudes, defined as the difference between the solar and zenithal ecliptic longitude for our specific observing site. The horizontal dashed line represents the absence of zodiacal light affecting the natural NSB measurements. The relationship between latitude and longitude in this blue-colored area is shown in Figure 6a. The vicinity of the ecliptic plane, indicated by a vertical green band, is shown enlarged in Figure 6b.

analyzed in Section 5.1, all measurements corresponding to the first 4 hr of the night have been removed. The NSB difference as a function of helioecliptic longitude and latitude is presented in Figure 5. As expected, there is a clear trend toward a fading of zodiacal light with increasing separation from the Sun and the ecliptic. We search for the ecliptic latitude at which the difference between m_{TESS} and $P50_{\text{TESS}}$ is near 0, indicated in the figure by a horizontal black dashed line. This is equivalent to finding the cutoff points between the horizontal blue band in the figure and each of the curves. All points above this band are considered to be unaffected by zodiacal light. The procedure, illustrated in Figure 6a, is as follows.

We restrict our data to the 28 darker photometers, corresponding to a $P50_{\text{TESS}} > 21.5$ mag/arcsec², and define a longitude bin size of 5° , which is wide enough to avoid fluctuations between the data as a consequence of having a small sample (around 20,000 measurements each), but still allow a good sampling of the latitude–longitude curve. For each bin, we seek the value of the ecliptic latitude for which the sky brightness difference is greater than 0, i.e., for which the zodiacal light effect is negligible. This value of ecliptic latitude for each helioecliptic longitude bin is represented in Figure 6a as a



(a) Relation between the helio-ecliptic longitude and latitude of the points where the condition $m_{\text{TESS}} - P50_{\text{TESS}} = 0$ is satisfied and the contribution of the zodiacal light is considered to be negligible. The corresponding filter is defined by the blue dashed line. Thus, all points in the blue area are considered to be clear of astronomical components.



(b) NSB difference versus helio-ecliptic longitude for zenithal observations near the ecliptic, i.e. with latitude $|\beta| < 20^\circ$. The brightness bump near the antisolar point corresponds to the Gegenschein.

Figure 6. Detail of the border region in ecliptic coordinates where the zodiacal light filter is defined (top), marked with a blue horizontal band in Figure 5, and the vicinity of the ecliptic (bottom), marked with a green vertical band in Figure 5. Each black dot corresponds to a bin of 5° in helio-ecliptic longitudes.

black dot. As we increase separation from the Sun, the ecliptic latitude from which zodiacal light begins to fade becomes smaller. This is what can be seen in brightness

maps such as those made by Kwon et al. (2004), with a broader distribution near the horizon at dusk and dawn that gradually narrows toward the antisolar point. The only exception is near this position, where the Gegenschein can be noticed. Indeed, Figure 6b shows the sky brightness difference as a function of helioecliptic longitude by adding up all the data for ecliptic latitude less than 20° (the vertical green band in Figure 5). The sudden increase in brightness from 165° onward should be noted; this is indicative of the detection of the Gegenschein with the TESS photometers. It is expected that for all points above the black ones in Figure 6a the contribution of zodiacal light is negligible. Hence, these points are used as a reference to set the ecliptic filter:

$$|\beta| > \max(105 - 0.45 \cdot |\lambda - \lambda_\odot|, 30) \quad (\text{deg}) \quad (2)$$

where the maximum condition is introduced to take into account the Gegenschein enhancement. This expression defines the set of ecliptic coordinates of the clear points, which is shown as a blue-highlighted area in Figure 6a.

3.3. Atmospheric components

3.3.1. Natural airglow

High-energy solar radiation incident on the upper atmosphere, around 90–100 km (mesopause) and 270 km (ionospheric F2 layer), leads to numerous photochemical processes that result in light emission known as airglow. These chemoluminescence processes are the result of the decay of excited states of atoms and molecules produced by chemical reactions (see Khomich et al. (2008) for a detailed description). In the visible band, airglow is characterized by a multicomponent pseudo-continuum with reactions of iron and nitric oxide, atomic oxygen, or ozone and several emission lines that dominate the night sky spectrum. For instance, the relaxation of atomic oxygen previously excited to the ^1S state in a two-step process involving O_2 , results in the spontaneous emission of a 5577 \AA photon (Barth & Hildebrandt 1961), which is the most prominent line and gives the airglow its characteristic green color. On the other hand, the common red color is mainly due to the forbidden-line emission by the dissociative recombination of $[\text{OI}] 6300$ in a higher layer of the atmosphere (250–300 km) and the relaxation of vibrationally excited OH radicals resulting from the ozone hydration process (Meinel 1950). Other lines, such as those of the Na I D doublet or molecular oxygen, can also be seen in the visible spectrum (Roach & Gordon 1973), some of them included in Figure 16.

While the astronomical components described in the previous section could be modeled quite accurately ow-

ing to their stationarity in their respective reference systems, airglow is not only highly variable but also difficult to predict. The brightness of airglow lines can vary by up to 20% in tens of minutes over a long temporal and spatial range. The numerous reactions that result in airglow can be affected by multiple factors, including solar activity, seasonal trends, changes in atmospheric variables or the composition of the upper layers, geomagnetic activity, gravity waves, and so forth (Khomich et al. 2008). Such a complex system makes it difficult to perform systematic processing of photometric data, so no filter is defined to model this. Moreover, airglow is considered an important element in natural NSB and will be discussed in the next sections.

3.3.2. Artificial skyglow

A non-negligible part of artificial outdoor lighting is emitted toward the sky directly or reflected from different surfaces, resulting in an increase in sky brightness known as skyglow (Falchi et al. 2016). Although changes in ground-based source emissions modulated by atmospheric scattering processes in the presence of dust particles, water droplets, and other atmospheric components can be reflected in the spectral properties of the diffuse light (e.g., Benn & Ellison (1998)), their counterpart in broadband photometers is not so obvious (Sánchez de Miguel et al. 2017). Particularly in dark locations with low outdoor lighting density, artificial skyglow is not expected to show short-term variations, but a stationary intensity, characteristic of each location, which constitutes the main driver of its darkness.

There is a possibility that NSB measurements show an abrupt change as a consequence of some modification in the nearby illumination that directly affects it. This is the case, for instance, of the photometer stars271, located in Puerto Villareal (Extremadura, Spain), whose data show a sudden brightening at the end of 2019 as a consequence of a new streetlight installed a few meters away from the device. The method described in this section permits not only the determination of the darkness of the site but also the identification of possible changes in the observational configuration from the distribution of its measurements or its statistical parameters. In this work, a 3σ clipping of the filtered data is applied to identify outliers.

4. NATURAL NIGHT SKY BRIGHTNESS

When determining the natural sky brightness of different observing sites and comparing studies, it is important to take into account the definition of the natural NSB used and the different filters or corrections applied to the raw data. With regard to the former, it is essential to reach a quantitative consensus on what is considered

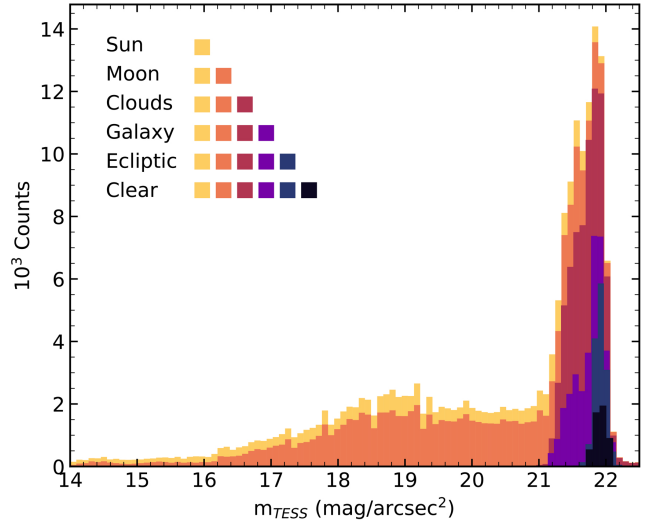


Figure 7. Histogram of the data measured by the stars90 photometer between 2018 December 21 and 2019 November 18 at ORM (La Palma). The components that affect the natural NSB have been filtered from the original 189,000 data obtained from $m_{\text{TESS}} = 14$ mag/arcsec² onward: sunlight (alt < -18° , 31,000), moonlight (alt < -5° , 85,000), clouds ($\sigma_{\text{TESS}} < 0.01$, 40,000), Galactic light ($|b| \geq 40^\circ$, 18,000) and zodiacal light (Equation (2), 10k), resulting in 5138 clear data (black) with $P50_{\text{TESS}} = 21.94 \pm 0.04$, $P99_{\text{TESS}} = 22.08 \pm 0.04$ and $\sigma_{\text{TESS}} = 0.08$ mag/arcsec².

natural NSB. For instance, the most common option is to take the arithmetic mean of all-sky brightness measurements taken over several nights (see, for example, Walker (1988); Pilachowski et al. (1989); Mattila et al. (1996); Krisciunas (1997); Sánchez et al. (2007); Pedani (2014); Plauchu-Frayn et al. (2017); Posch et al. (2018)). Other authors also include the minimum and maximum values as a reference for natural NSB take into account the seasonal variations produced, for example, by solar activity (Duriscoe et al. 2007; Patat 2008). In this direction, Leinert et al. (1998) considered the minimum/maximum values as the average of the three smallest/largest sky brightness values (nightly averages) given for each site. We consider that the natural NSB of a site should be understood from a probabilistic point of view, quantifying the frequency with which a given sky brightness value occurs during the dark period—after filtering the data from the components described in Section 3—using percentiles, as done by Benn & Ellison (1998), Kornilov et al. (2016), Yang et al. (2017), and Aubé et al. (2020). In this work, we have taken the P50 and P99 percentiles of the filtered data set as indicators of the median and maximum darkness, as shown in Table 2 together with the standard deviation. In total, 44 photometers are included, after the constraint

Table 1. Percentile 50 and 99 of Zenithal NSB for ASTMON and TESS Measurements at ORM and OT during 2019–2020.

Band	P50 (ORM)	P99 (ORM)	Data (ORM)	P50 (OT)	P99 (OT)	Data (OT)
	(mag/arcsec ²)	(mag/arcsec ²)	raw (filtered)	(mag/arcsec ²)	(mag/arcsec ²)	raw (filtered)
<i>B</i>	22.36 ± 0.03	22.62 ± 0.03	4224 (181)	22.05 ± 0.03	22.32 ± 0.03	2236 (59)
<i>V</i>	21.66 ± 0.02	21.89 ± 0.02	4217 (173)	21.22 ± 0.03	21.51 ± 0.02	2227 (91)
<i>R</i>	20.92 ± 0.01	21.13 ± 0.01	4193 (171)	20.72 ± 0.01	21.09 ± 0.01	2078 (88)
<i>m</i> _{TESS}	21.94 ± 0.04	22.08 ± 0.04	179796 (5140)	21.34 ± 0.04	21.53 ± 0.04	430,993 (8101)

NOTE—Only filtered data (see section 3 for details) has been used to calculate final magnitude values.

of having at least 1000 filtered data and a percentage of clear night time greater than 30% is imposed.

The best value for the natural NSB (i.e., the pristine night sky) for the Johnson–Cousins *BVR* photometric system (Bessell 1990), of the moonless sky on a clear night at high ecliptic and Galactic latitudes and during solar minimum is typically 22.7 mag/arcsec² in *B*, 21.9 mag/arcsec² in *V*, and 21.1 mag/arcsec² in *R* (Hänel et al. 2018). For the SQM, the value of 22 mag/arcsec² is taken as a reference (Falchi et al. 2016). For all the photometers, the percentiles have been calculated from the distribution resulting from applying the filters explained in Section 3. The result of this analysis is shown in Figure 7 for stars90 at ORM. Taking P50 as the reference of the natural NSB, this is the darkest of all the sites analyzed in this work (P50 = 21.94 ± 0.04 mag/arcsec²), and it is assumed that its NSB is, in the best atmospheric conditions, very close to the natural one.

The natural NSB at ORM was measured on 427 CCD images taken with the Isaac Newton and Jacobus Kapteyn Telescopes on 63 photometric nights between 1987 and 1996 by Benn & Ellison (1998) (hereafter). The sky brightness at high elevation (elev. > 45°), high Galactic latitude ($|\beta| > 10^\circ$), high ecliptic latitude ($|\beta| > 40^\circ$), solar minimum (1994–1996) and moonless nights was $B = 22.70 \pm 0.03$ mag/arcsec², $V = 22.00 \pm 0.03$ mag/arcsec², $R = 21.00 \pm 0.03$ mag/arcsec². To make comparisons with these standard bands, we have also used the measurements taken by the ASTMON (Aceituno et al. 2011) located at ORM, contemporaneously with the clear data from the stars90 photometer. Table 1 shows the P50/P99 zenithal NSB measurements using both devices. The new results are consistent with the BE98 measurements in *B*. In the *R* band, the P99 measurement is darker than the BE98 estimate (+0.13 mag/arcsec²), while *V* is slightly brighter

(−0.11 mag/arcsec²). The ORM NSB decreases in the *R* band since the BE98 result is probably due to the significant change in lighting systems on the island of La Palma. From 1987 to 1996, a large number of low-pressure sodium lamps emitted only in the *R* band. The effect is the opposite in the *V* band, which is influenced by new LED lighting systems (Aubé et al. 2020). To summarize, *BVR* measurements by ASTMON and mTESS measurements by TESS at ORM may be considered unpolluted, as artificial light adds only approximately 2% to the natural NSB. This is a result similar to that of the Hawaiian Observatories (Wainscoat 2018). On the other hand, night skies at OT are moderately polluted (−0.31 in *B*, −0.44 in *V*, −0.2 in *R* and −0.6 in *m*_{TESS}, mag/arcsec² units), which is consistent with the exhaustive analysis conducted by Aubé et al. (2020). In the case of the San Pedro Martir Observatory (Mexico), measurements made by stars213 during 2018–2020 show a P50_{TESS} of 21.77 ± 0.04 mag/arcsec², which is also consistent with the average *m*_{SQM} = 21.72 mag/arcsec² measured in 2016 by Plauchu-Frayn et al. (2017).

For a given location, there are nights of the year when zenithal brightness measurements are inevitably influenced by the different astronomical components. Figure 8 shows the difference in sky brightness for different positions (α , δ) in the sky. Since the zenith decl. is the same as the geographical latitude of the site, each device completes a horizontal line throughout the year. All clear data have been averaged in bins of approximately 1^h in R.A. and 5° in decl. On the upper axis, the months have been placed as a reference, taking for this purpose the R.A. of the zenith in the middle of the night, i.e., the sidereal time when the Sun is at lower culmination. It is noted that the best time to measure the zenithal natural NSB is during local spring, as the available time is longer. In the earlier months, measurements can be taken at the end of the night (higher R.A.) while the opposite applies in the later months. At equatorial lati-

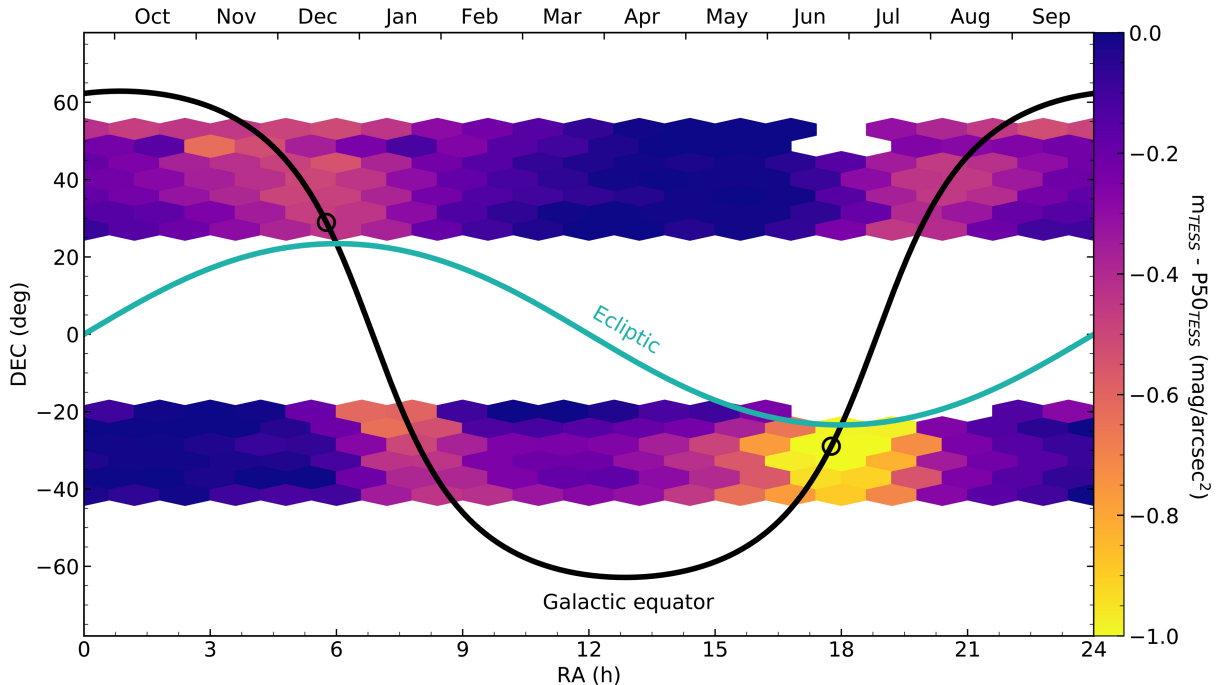


Figure 8. NSB difference for a given celestial position (R.A., decl.). The upper axis includes the reference months, corresponding to the R.A. of the zenith at the midpoint of the night, i.e., the sidereal time when the Sun is at lower culmination. The Galactic equator (black) and the ecliptic (green) are also included. The black rings around $(-18^{\text{h}}, -30^{\circ})$ and $(6^{\text{h}}, 30^{\circ})$ mark the Galactic center and anticenter, respectively.

tudes, the presence of the ecliptic at the zenith makes it impossible to make these measurements, which will always be affected by zodiacal light. Furthermore, around the solstices the Galaxy will be present, especially in the southern winter, where the Galactic center will be very high at midnight.

5. DISCUSSION. TEMPORAL VARIATIONS

Many factors that can contribute to the determination of the natural darkness of a particular site have been ignored in the method presented here. For instance, near-desert locations (e.g., Namibia, Canary Islands, and Israel) could be affected by the circulation of dust in the atmosphere (Sciezor 2020). The presence of fires (e.g., in Australia) can also affect NSB measurements, as well as aerosols from anthropogenic activity in nearby urban areas (e.g., in Extremadura, Balearic Islands, and Arizona). ALAN may determine, of course, the median sky brightness and could also hide some of the variations presented (see Puschnig et al. (2020)). Nevertheless, the use of differential photometry and the combination of many photometers placed in dark locations make it possible to highlight emergent properties by allowing a statistical characterization of the natural NSB. As a matter of fact, all the sites present a standard deviation very close to 0.1 mag/arcsec^2 (see Table 2), which may

indicate that there is a main mechanism driving the variability of NSB measurements in very dark sites.

The timescale has been investigated in order to study the possible origin of this variability. Figure 9 shows the distribution of the standard deviation grouping of the data for each photometer over different time intervals, from minutes to months. Both hemispheres have been separated to check that there is no apparent bias between them. If the total variability of 0.1 mag/arcsec^2 were of an instrumental nature (some undetected instrumental error of the device), it would be expected to be reached at intervals of tens of minutes. However, at intervals of 1 hr the median σ_{TESS} is $0.014 \text{ mag/arcsec}^2$ and at the minute timescale it is below $0.004 \text{ mag/arcsec}^2$, compatible with the instrumental error obtained in laboratory tests (see A.2). The intranight variability, with a median standard deviation of less than $0.04 \text{ mag/arcsec}^2$, cannot explain the average 0.1 mag/arcsec^2 , but its nature deserves to be explained in more detail in the following sections.

5.1. Dusk enhancement. Walker effect

One option for this intranight variability is the possible post-twilight effects first identified by Walker (1988). Using measurements made in the B and V filters from

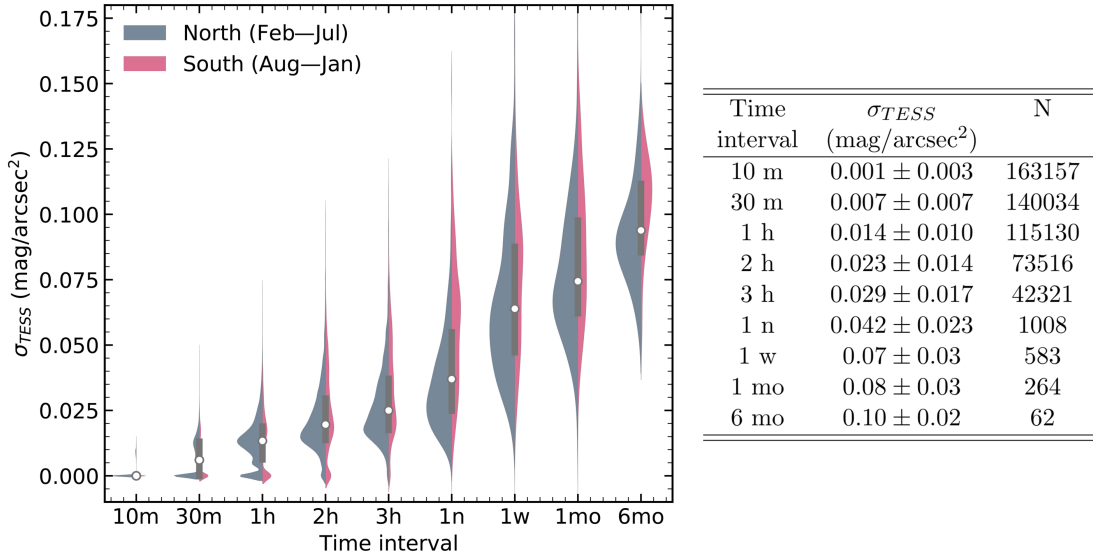


Figure 9. Distributions of the standard deviation σ_{TESS} calculated from individual photometer measurements grouped in different time intervals: minutes (m), hours (h), nights (n), weeks (w), and months (mo). The northern and southern hemispheres, corresponding to different periods of the year, have been divided to check that there is no clear difference between them. Over the histograms, the mean (white dot) and the standard deviation (black box) of the distributions have been added. For the sake of clarity, these values are shown in the supplementary table together with the total number of samples, N, in each interval.

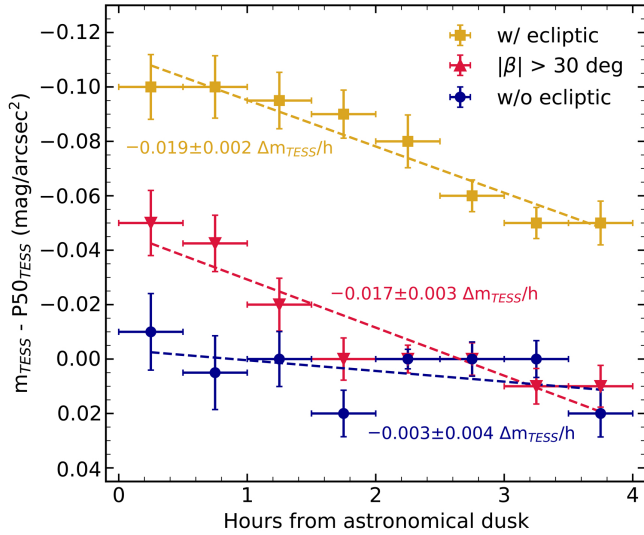


Figure 10. NSB difference vs. time elapsed from the end of astronomical twilight at the beginning of the night for data fully filtered with the method proposed in this work (blue), for filtering of zodiacal light from absolute elliptical latitudes higher than 30° (red), and for no filtering at all (yellow). Fit lines and their slopes are included.

San Benito Mountain during the period 1976–87, he found an exponential decrease of the NSB of up to 0.4 mag/arcsec^2 during the first 4 hr of the night, which he identified with a process of recombination of ions excited during the day by extreme ultraviolet solar radiation. Since then, many authors have addressed this issue at

different sites and times within the solar cycle. Taylor et al. (2004) reported a decrease of 0.2, 0.3, 0.3, and 0.4 mag/arcsec^2 throughout the night by observations in the *UBVR* filters, respectively, from 1999 to 2003 at Mount Graham, although their result was later refuted by Pedani (2009), who found no trend in a twice-larger sample taken at the same location. Measurements of zenith NSB in the *UBVRI* filters taken at Calar Alto by Leinert et al. (1995), at La Palma by Benn & Ellison (1998), at Cerro Paranal by Patat (2003), and at San Pedro Martir by Plauchu-Frayn et al. (2017) also show no evidence of a systematic nightly NSB decrease after astronomical twilight.

A much smoother trend of 0.03 mag/hr was found by Krisciunas (1997) in observations in *B* and *V*, close to the 0.01 ± 0.01 and $0.02 \pm 0.01 \text{ mag/hr}$, respectively, in the review of Walker’s data conducted by Patat (2003). Both took into account the solar activity cycles and introduced corrections for the zodiacal light contribution from the Levasseur-Regourd & Dumont (1980) model. While the exponential decrease found by Walker has already been largely ruled out—it is probably associated with light pollution (Garstang 1997) or solar cycle effects—this smooth trend has not. In Figure 10 we have plotted the variation of the NSB measurements as a function of time from the end of astronomical twilight. In the data completely filtered by the method explained in Section 3 (blue dots), no clear trend toward a darkening of the sky during the first hours of

the night is observed. The slope of the fitted line is $0.003 \pm 0.004 m_{\text{TESS}}/\text{hr}$ compatible with 0. The plot also includes the data for completely unfiltered zodiacal light (yellow squares) and that filtered at a constant absolute ecliptic latitude of 30° . Note that although the former shows, as expected, a higher brightening than the latter, both have similar trends of 0.019 ± 0.002 and $0.017 \pm 0.003 m_{\text{TESS}}/\text{hr}$, which are also compatible with those reported by [Krisciunas \(1997\)](#) and [Patat \(2003\)](#). As shown in [Figure 10](#), in spite of its increasing separation from the Sun in the early night, the contribution of zodiacal light is smaller, resulting in a gradual darkening during the first hours, especially in the *B*, *V*, and *R* filters, where the zodiacal light spectrum reaches its peak.

5.2. Short-time variations

On hourly timescales, the variability may be due to the passage of brighter or fainter star fields through the FOV of the photometer, or to variations in airglow or skyglow scattering throughout the night. In the former case, a star field would take less than 1.5 hr to cross the entire FOV, so no difference should be seen between the distributions at 2 hr, 3 hr, and 1 night in [Figure 9](#), although a progressive increase in σ_{TESS} is observed. Furthermore, the same pattern should be seen on two consecutive nights with a 4 minute delay in the same photometer, which has not been found in general. Some authors have identified particular nights when short-period variations were present both in broadband photometry ([Leinert et al. 1998](#); [Pilachowski et al. 1989](#); [Patat 2003](#)) and in specific lines characteristic of airglow emissions ([Patat 2008](#)). In this work, we report the systematic observation of short-time variations in NSB (tens of minutes and hours) on the vast majority of nights and regardless of the geographical position, fraction of the night, and season of the year.

An example of these variations is shown in [Figure 11](#), which includes data from three photometers located in Australia between 13 and 15:30 UT on 2019 October 28. The stars298 (red) and stars311 (yellow) devices, located 6.3 km apart, show very similar behavior, with a quasiperiodic oscillation of about 1 hr. The stars345 device (blue), located more than 90 km away from them, shows similar behavior at the beginning and end of the interval, but does not follow the brightening that occurs in the other two at around 14.5 UT. This can be seen in the difference between the stars345 and stars311 measurements with respect to stars298, which is plotted below. The dispersion between the photometers at 93.4 km is larger than the dispersion between those at 6.3

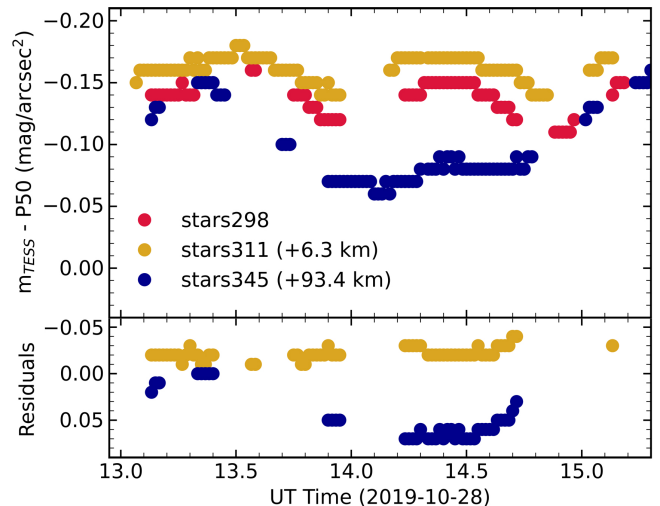


Figure 11. Short-time variations of NSB on the night of 2019 October 28 for three photometers located in Australia, two of them separated by 6.3 km and the other by 93.4 km. The lower plot shows the differences between the photometers stars311 (yellow) and stars345 (blue) with respect to stars298 (red).

km, whose NSB curves show very similar. This is not a serendipitous result. With an FOV (FWHM) of 17° , two photometers close enough to each other can see the same phenomenon occurring at a certain height depending on the distance between them. In this case, we say that the photometers are coherent and we can try to estimate the height at which these short-time events occur by the geometric parallax.

For this purpose, pairs of all available photometers have been taken. Each night, we obtain the difference between simultaneous measurements of both (at most 30 s apart) and determine their standard deviation. The final value for each pair and its uncertainty is obtained by averaging all the nights and calculating the standard error. The result for all the photometers against their separation is shown in [Figure 12](#). The moving average of all points (shaded) and the geometric parallax height corresponding to each distance, obtained by simple trigonometry, are included (effects of curvature, refraction, etc., have been neglected as they do not affect this discussion). There are two differentiated regions.

At long separations, beyond 150–200 km, the standard deviation of the difference between their measurements shows a stationary trend around $0.03 \text{ mag}/\text{arcsec}^2$ and very high dispersion. This is a consequence of the loss of coherence between the photometers, whose NSB measurements are not correlated as they do not observe the same projected region where the disturbances are occur-

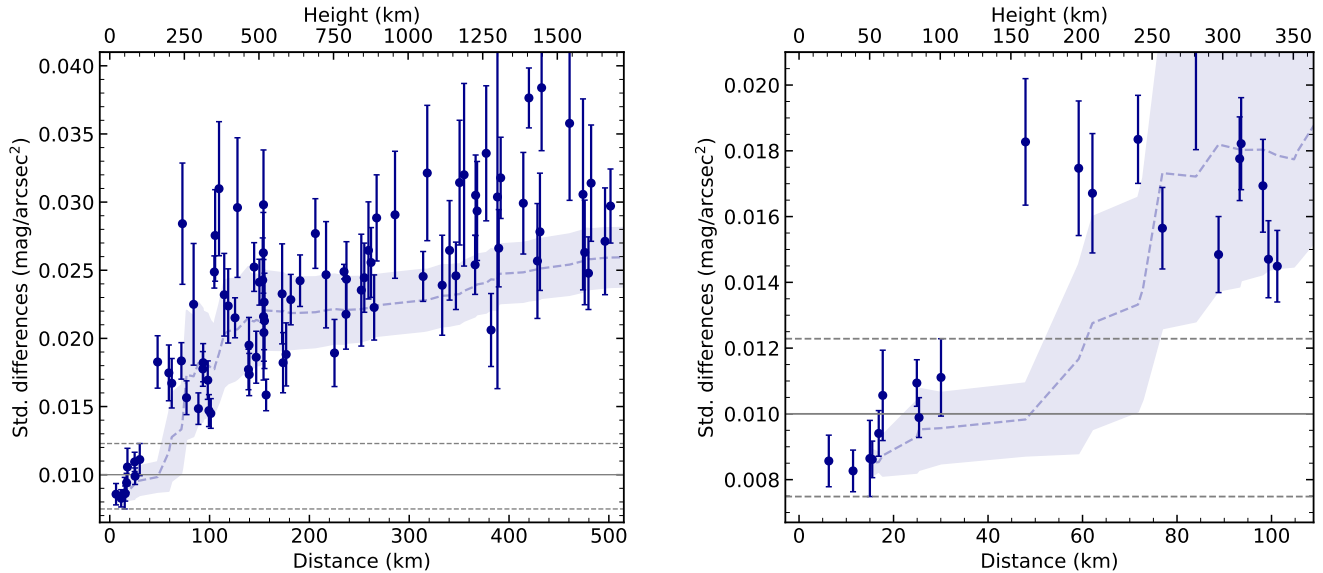


Figure 12. Standard deviation of the difference between simultaneous measurements of pairs of photometers vs. their separation. The geometric parallax height is indicated on the upper axis. The moving average and the 3σ limit are shown shaded and the coherence region is indicated by black horizontal lines. Points of closer pairs (less than 100 km) are zoomed in on the right plot.

ring. Note that the value of these standard deviations is compatible with that obtained for the sky variation in 3 hr⁻¹ night intervals in Figure 9, which reinforces the idea that photometers far apart from each other are not coherent and measure different NSB variations. The differences between photometers separated by less than 30 km, on the other hand, show a very low dispersion, around 0.01 mag/arcsec² (see Figure 12), which is compatible with that obtained for the three adjacent photometers of OT (Figure 15). The existence of coherence between photometers located less than 30 km apart has a very relevant implication: the phenomena observed simultaneously, which are the origin of the short-time variations, are occurring at a height of at least 100 km. If these variations were due to tropospheric events such as clouds, aerosols, turbulence, etc., no coherence would be observed between photometers separated by more than 3 km. From this discussion we therefore conclude that the shortterm NSB variations observed with the photometers are produced by luminous phenomena that take place above the mesosphere, i.e., airglow.

5.3. Seasonal variations

Following the analysis of Figure 9, the total standard deviation of 0.1 mag/arcsec² only seems to be reached on monthly or annual scales. Several reasons could explain this. One such reason is the dependence of the natural NSB on the season of the year, which was identified by Patat (2008) in both *BVRI* filters and airglow lines. To test this, in Figure 13 we have plotted

our measurements with respect to the day of the year, grouping them into nights, weeks, and months. A semi-annual trend similar to that observed by Patat in the R and V filters seems to be suggested, with a brightening near the equinoxes and a darkening near the solstices of amplitude 0.1 mag/arcsec², especially remarkable in the months of December and January. In these regions of the spectrum, the airglow lines of [OI] 5577 and [OI] 6300 (see Figure 16) also show this variability (Figures 9 and 10 in Patat (2008)). Thus, the dispersion of 0.1 mag/arcsec² observed in all the photometers could be due to variability in the airglow intensity on scales of weeks or months. Its nature is still under study.

There may be other reasons for this yearly variability. The possibility that the TESS photometers suffer from aging effects is on the table. The only systematic study of this with SQM + window devices is the recent one by Puschnig et al. (2021), which suggests that a darkening of up to 0.053 m_{SQM} arcsec⁻² yr⁻¹ can occur at midlatitudes. However, we do not observe evidence of this behavior in the continuous measurements of the TESS photometers or any bias in the distributions of photometers manufactured in different years. Further work should be done on this matter.

The fact that, over long timescales, it is possible to detect an overall increase in natural brightness as a consequence of the increase in light pollution, quantified at 2.2% by Kyba et al. (2017), cannot be ignored either

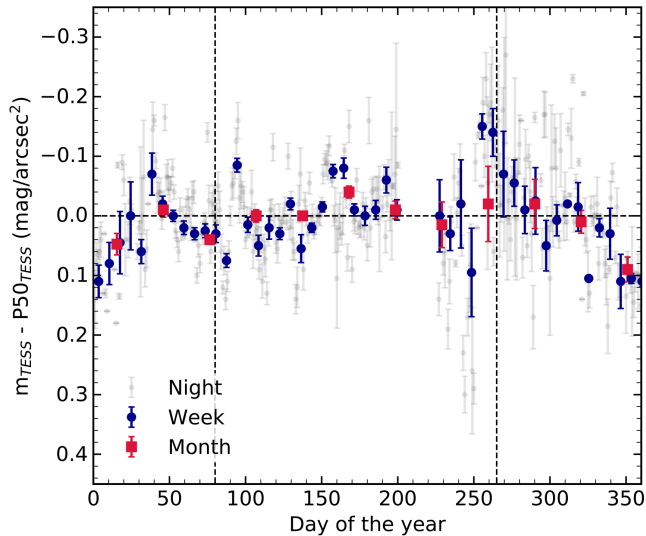


Figure 13. NSB difference vs. day of the year since January 1 with data averaged over night (gray), week (blue), and month (red) intervals. Equinoxes are indicated by vertical dashed lines.

and requires a more detailed examination over a longer period.

On the other hand, it is known that solar activity can affect NSB by establishing peak-to-peak differences of up to 0.5 mag in B and V during a solar cycle (Walker 1988; Leinert et al. 1995; Mattila et al. 1996; Krisciunas 1997; Benn & Ellison 1998; Patat 2008; Plauchu-Frayn et al. 2017). One of the most widely used proxies to determine the relation between solar activity and NSB measurements is the solar flux at 10.7 cm. The correlation has been checked by taking different time delays and no conclusive trend has been found. This does not mean that it cannot be detected with broadband photometers, but it is a consequence of the quiescence of the Sun at minimum, when the range of F10.7 cm intensities is too low to check these relations. More measurements will be accumulated in the coming years to try to verify this relationship.

6. CONCLUSIONS

This article has attempted to study natural NSB using data from dozens of TESS photometers at more than 40 sites with almost pristine skies during the solar minimum between Solar Cycles 24 and 25. The main conclusions of this work may be summarized as follows:

- The first comprehensive reference method to measure the natural NSB with low-cost broadband photometers has been defined.
- Differential photometry allows very high accuracies to be achieved by combining different broad-

band photometers in search of emerging properties.

- The usefulness of the ROC curve has been demonstrated, together with that of the standard deviation method, for determining the most appropriate threshold for cloud detection and its uncertainties.
- Moonlight can contribute to the NSB measurement if its elevation is higher than -5° .
- Galactic light can increase the NSB if it is measured at an absolute latitude less than 40° and approximately homogeneously for all longitudes.
- The heliocentric longitude has to be taken into account in dealing with zodiacal light, and the possibility of detecting the Gegenschein with broadband photometers has been demonstrated for the first time.
- The natural NSB has been calculated from the percentiles for 44 different photometers, the ORM ones being the darkest of all of them.
- A standard deviation around 0.1 mag/arcsec^2 is observed in all the photometers, owing to NSB variations on scales up to months.
- The so-called Walker effect has been reviewed and no evidence has been found for systematic darkening during the first hours of the night. This effect is compatible with an insufficient subtraction of zodiacal light.
- We report the systematic observation of short-time variations in NSB on the vast majority of nights that are related to airglow events forming above the mesosphere.
- There are indications of semiannual oscillations compatible with what has been previously observed in airglow emission features by other authors.

Future work should address possible aging effects and relations of the natural NSB with solar and geomagnetic phenomena. Distinguishing between the main components of the airglow observed with TESS photometers and describing their structure or dynamics requires, on the one hand, devices with a narrower spectral range centered on the main emission features and, on the other hand, better sampling of the transition region between coherent and noncoherent photometers (following the definition given in this work). The installation of photometer networks with high temporal resolution separated by tens of kilometers in very dark locations is highly desirable.

EELabs is a project funded by the European Union through INTERREG V-A MAC 2014–2020.

STARS4ALL was a project funded by the European Union through H2020-ICT- 2015-688135. We thank the referee for constructive suggestions. We thank Javier Díaz Castro and Federico de la Paz (Oficina Técnica de Protección del Cielo, IAC) for maintaining the ASTMON devices and Julio A. Castro Almazán for processing the ASTMON data. The AMOS Canary Islands facility of the Department of Astronomy, Earth Physics,

and Meteorology of Comenius University (Bratislava, Slovakia) provided us with all-sky meteor images for cloud coverage analysis validation. The High Energy Stereoscopic System Observatory (H.E.S.S., Namibia), Hakos Astrofarm (Namibia), and Extremadura Clear Skies are thanked for hosting TESS photometer networks.

REFERENCES

- Aceituno, J., Sánchez, S. F., Aceituno, F. J., et al. 2011, *Publications of the Astronomical Society of the Pacific*, 123, 1076, doi: [10.1086/661918](https://doi.org/10.1086/661918)
- Aubé, M., Simoneau, A., Muñoz-Tuñón, C., Díaz-Castro, J., & Serra-Ricart, M. 2020, *MNRAS*, 497, 2501, doi: [10.1093/mnras/staa2113](https://doi.org/10.1093/mnras/staa2113)
- Bará, S., Tapia, C., & Zamorano, J. 2019, *Sensors*, 19, 1336, doi: [10.3390/s19061336](https://doi.org/10.3390/s19061336)
- Barth, C. A., & Hildebrandt, A. F. 1961, *J. Geophys. Res.*, 66, 985, doi: [10.1029/JZ066i003p00985](https://doi.org/10.1029/JZ066i003p00985)
- Benn, C., & Ellison, S. 1998, *New Astronomy Reviews*, 42, 503, doi: [10.1016/s1387-6473\(98\)00062-1](https://doi.org/10.1016/s1387-6473(98)00062-1)
- Bennie, J., Davies, T. W., Cruse, D., & Gaston, K. J. 2016, *Journal of Ecology*, 104, 611
- Bessell, M. S. 1990, *PASP*, 102, 1181, doi: [10.1086/132749](https://doi.org/10.1086/132749)
- Bustamante-Calabria, M., Sánchez de Miguel, A., Martín-Ruiz, S., et al. 2021, *Remote Sensing*, 13, 258, doi: [10.3390/rs13020258](https://doi.org/10.3390/rs13020258)
- Cavazzani, S., Ortolani, S., Bertolo, A., et al. 2020, *MNRAS*, 493, 2463, doi: [10.1093/mnras/staa416](https://doi.org/10.1093/mnras/staa416)
- Cinzano, P. 2007, doi: [10.13140/RG.2.2.35630.51526](https://doi.org/10.13140/RG.2.2.35630.51526)
- de Miguel, A. S., Kyba, C. C. M., Zamorano, J., Gallego, J., & Gaston, K. J. 2020, *Scientific Reports*, 10, doi: [10.1038/s41598-020-64673-2](https://doi.org/10.1038/s41598-020-64673-2)
- Duriscoe, D. M. 2013, *PASP*, 125, 1370, doi: [10.1086/673888](https://doi.org/10.1086/673888)
- Duriscoe, D. M., Luginbuhl, C. B., & Moore, C. A. 2007, *PASP*, 119, 192, doi: [10.1086/512069](https://doi.org/10.1086/512069)
- Falchi, F., Cinzano, P., Duriscoe, D., et al. 2016, *Science Advances*, 2, e1600377, doi: [10.1126/sciadv.1600377](https://doi.org/10.1126/sciadv.1600377)
- Gallaway, T. 2010, *Journal of Economic Issues*, 44, 71. <http://www.jstor.org/stable/40647711>
- Garstang, R. H. 1997, in *American Astronomical Society Meeting Abstracts*, Vol. 190, American Astronomical Society Meeting Abstracts #190, 04.04
- Gaston, K. J., Bennie, J., Davies, T. W., & Hopkins, J. 2013, *Biological reviews*, 88, 912
- Gill, A., Benton, S. J., Brown, A. M., et al. 2020, *AJ*, 160, 266, doi: [10.3847/1538-3881/abbffb](https://doi.org/10.3847/1538-3881/abbffb)
- Hänel, A., Posch, T., Ribas, S. J., et al. 2018, *Journal of Quantitative Spectroscopy and Radiative Transfer*, 205, 278, doi: [10.1016/j.jqsrt.2017.09.008](https://doi.org/10.1016/j.jqsrt.2017.09.008)
- Hoffmann, B., Tappert, C., Schlosser, W., et al. 1998, *A&AS*, 128, 417, doi: [10.1051/aas:1998389](https://doi.org/10.1051/aas:1998389)
- Hölker, F., Wolter, C., Perkin, E. K., Tockner, K., et al. 2010, *Trends in ecology & evolution*, 25, 681
- Jechow, A., Hölker, F., & Kyba, C. C. M. 2019, *Scientific Reports*, 9, 1391, doi: [10.1038/s41598-018-37817-8](https://doi.org/10.1038/s41598-018-37817-8)
- Jechow, A., Kolláth, Z., Ribas, S. J., et al. 2017, *Scientific Reports*, 7, 6741, doi: [10.1038/s41598-017-06998-z](https://doi.org/10.1038/s41598-017-06998-z)
- Jones, A., Noll, S., Kausch, W., Szyszka, C., & Kimeswenger, S. 2013, *A&A*, 560, A91, doi: [10.1051/0004-6361/201322433](https://doi.org/10.1051/0004-6361/201322433)
- Khomich, V. Y., Semenov, A. I., & Shefov, N. N. 2008, *Airglow as an Indicator of Upper Atmospheric Structure and Dynamics* (Springer-Verlag Berlin Heidelberg)
- Kornilov, V., Kornilov, M., Voziakova, O., et al. 2016, *MNRAS*, 462, 4464, doi: [10.1093/mnras/stw1839](https://doi.org/10.1093/mnras/stw1839)
- Krisciunas, K. 1997, *PASP*, 109, 1181, doi: [10.1086/133993](https://doi.org/10.1086/133993)
- Kwon, S. M., Hong, S. S., & Weinberg, J. L. 2004, *NewA*, 10, 91, doi: [10.1016/j.newast.2004.05.004](https://doi.org/10.1016/j.newast.2004.05.004)
- Kyba, C. C. M., Ruhtz, T., Fischer, J., & Hölker, F. 2011, *PLoS ONE*, 6, e17307, doi: [10.1371/journal.pone.0017307](https://doi.org/10.1371/journal.pone.0017307)
- Kyba, C. C. M., Kuester, T., de Miguel, A. S., et al. 2017, *Science Advances*, 3, e1701528, doi: [10.1126/sciadv.1701528](https://doi.org/10.1126/sciadv.1701528)
- Leinert, C., Vaisanen, P., Mattila, K., & Lehtinen, K. 1995, *A&AS*, 112, 99
- Leinert, C., Bowyer, S., Haikala, L. K., et al. 1998, *A&AS*, 127, 1, doi: [10.1051/aas:1998105](https://doi.org/10.1051/aas:1998105)
- Levasseur-Regourd, A. C., & Dumont, R. 1980, *A&A*, 84, 277
- Masana, E., Carrasco, J. M., Bará, S., & Ribas, S. J. 2021, *MNRAS*, 501, 5443, doi: [10.1093/mnras/staa4005](https://doi.org/10.1093/mnras/staa4005)
- Mattila, K., Vaeisaenen, P., & Appen-Schnur, G. F. O. V. 1996, *A&AS*, 119, 153
- Meinel, I. A. B. 1950, *ApJ*, 111, 555, doi: [10.1086/145296](https://doi.org/10.1086/145296)
- Mellinger, A. 2009, *PASP*, 121, 1180, doi: [10.1086/648480](https://doi.org/10.1086/648480)

- Noll, S., Kausch, W., Barden, M., et al. 2012, *A&A*, 543, A92, doi: [10.1051/0004-6361/201219040](https://doi.org/10.1051/0004-6361/201219040)
- Owens, A. C., & Lewis, S. M. 2018, *Ecology and evolution*, 8, 11337
- Patat, F. 2003, *A&A*, 400, 1183, doi: [10.1051/0004-6361:20030030](https://doi.org/10.1051/0004-6361:20030030)
- Patat, F. 2008, *Astronomy & Astrophysics*, 481, 575, doi: [10.1051/0004-6361:20079279](https://doi.org/10.1051/0004-6361:20079279)
- Patat, F., Ugolnikov, O. S., & Postlyakov, O. V. 2006, *A&A*, 455, 385, doi: [10.1051/0004-6361:20064992](https://doi.org/10.1051/0004-6361:20064992)
- Pedani, M. 2009, *PASP*, 121, 778, doi: [10.1086/603605](https://doi.org/10.1086/603605)
- . 2014, *NewA*, 28, 63, doi: [10.1016/j.newast.2013.10.005](https://doi.org/10.1016/j.newast.2013.10.005)
- Pilachowski, C. A., Africano, J. L., Goodrich, B. D., & Binkert, W. S. 1989, *Publications of the Astronomical Society of the Pacific*, 101, 707, doi: [10.1086/132494](https://doi.org/10.1086/132494)
- Plauchu-Frayn, I., Richer, M. G., Colorado, E., et al. 2017, *PASP*, 129, 035003, doi: [10.1088/1538-3873/129/973/035003](https://doi.org/10.1088/1538-3873/129/973/035003)
- Posch, T., Binder, F., & Puschnig, J. 2018, *JQSRT*, 211, 144, doi: [10.1016/j.jqsrt.2018.03.010](https://doi.org/10.1016/j.jqsrt.2018.03.010)
- Puschnig, J., Näslund, M., Schwöpe, A., & Wallner, S. 2021, *MNRAS*, 502, 1095, doi: [10.1093/mnras/staa4019](https://doi.org/10.1093/mnras/staa4019)
- Puschnig, J., Wallner, S., & Posch, T. 2020, *MNRAS*, 492, 2622, doi: [10.1093/mnras/stz3514](https://doi.org/10.1093/mnras/stz3514)
- Roach, F. E., & Gordon, J. L. 1973, *The light of the night sky.*, Vol. 4
- Rogan, W. J., & Gladen, B. 1978, *Am. J. Epidemiol*, 107, 71, doi: <https://doi.org/10.1093/oxfordjournals.aje.a112510>
- Sánchez, S. F., Aceituno, J., Thiele, U., Pérez-Ramírez, D., & Alves, J. 2007, *PASP*, 119, 1186, doi: [10.1086/522378](https://doi.org/10.1086/522378)
- Sánchez de Miguel, A., Aubé, M., Zamorano, J., et al. 2017, *MNRAS*, 467, 2966, doi: [10.1093/mnras/stx145](https://doi.org/10.1093/mnras/stx145)
- Schuerman, D. W., Weinberg, J. L., & Beeson, D. E. 1977, in *Bulletin of the American Astronomical Society*, Vol. 9, 313
- Sciezor, T. 2020, *JQSRT*, 247, 106962, doi: [10.1016/j.jqsrt.2020.106962](https://doi.org/10.1016/j.jqsrt.2020.106962)
- Spitschan, M., Aguirre, G. K., Brainard, D. H., & Sweeney, A. M. 2016, *Scientific Reports*, 6, 26756, doi: [10.1038/srep26756](https://doi.org/10.1038/srep26756)
- Swets, J. 1988, *Science*, 240, 1285, doi: [10.1126/science.3287615](https://doi.org/10.1126/science.3287615)
- Taylor, V. A., Jansen, R. A., & Windhorst, R. A. 2004, *PASP*, 116, 762, doi: [10.1086/422929](https://doi.org/10.1086/422929)
- Wainscoat, R. J. 2018, in *American Astronomical Society Meeting Abstracts*, Vol. 231, American Astronomical Society Meeting Abstracts #231, 142.02
- Walker, M. F. 1970, *PASP*, 82, 672, doi: [10.1086/128945](https://doi.org/10.1086/128945)
- Walker, M. F. 1988, *Publications of the Astronomical Society of the Pacific*, 100, 496, doi: [10.1086/132197](https://doi.org/10.1086/132197)
- Weinberg, J. L., Hanner, M. S., Beeson, D. E., DeShields, L. M., I., & Green, B. A. 1974, *J. Geophys. Res.*, 79, 3665, doi: [10.1029/JA079i025p03665](https://doi.org/10.1029/JA079i025p03665)
- Yang, Y., Moore, A. M., Krisciunas, K., et al. 2017, *AJ*, 154, 6, doi: [10.3847/1538-3881/aa73dc](https://doi.org/10.3847/1538-3881/aa73dc)
- Zamorano, J., García, C., Tapia, C., et al. 2017a, *International Journal of Sustainable Lighting*, 18, 49, doi: [10.26607/ijsl.v18i0.21](https://doi.org/10.26607/ijsl.v18i0.21)
- Zamorano, J., Tapia, C., García, C., et al. 2017b, in *Light Pollution: Theory, Modelling and Measurements*. https://guaix.ucm.es/wp-content/uploads/2020/02/2017_06_LPTMM_poster_TESS_calibration.pdf
- Zigo, P., Toth, J., & Kalmancok, D. 2013, in *Proceedings of the International Meteor Conference, 31st IMC*, La Palma, Canary Islands, Spain, 2012, ed. M. Gyssens & P. Roggemans, 18–20
- Zou, H., Zhou, X., Jiang, Z., et al. 2010, *AJ*, 140, 602, doi: [10.1088/0004-6256/140/2/602](https://doi.org/10.1088/0004-6256/140/2/602)

Table 2. Coordinates, Elevations, and Locations of TESS Photometers, Ordered by NSB (P50).

Name	Place	Latitude (deg)	Longitude (deg)	Alt. (m)	Tot1 (raw)	Tot2 (fil.)	P50 ± 0.04	P99 ± 0.04	σ	CNT (%)	Dates (yyyy-mm-dd)
stars90	ORM-IAC (La Palma,Spain)	28.76391	-17.89367	2152	189184	5138	21.94	22.08	0.08	77 ⁺⁴	2018-12-21 2019-11-18
stars298	EPSO (New South Wales,Australia)	-31.26010	149.22090	566	169564	3940	21.89	22.08	0.1	51 ⁺³	2019-05-12 2020-07-11
stars343	Woblesock Obs. (New South Wales,Australia)	-31.22690	149.33450	574	189883	4313	21.87	22.07	0.1	55 ⁺³	2019-06-07 2020-05-08
stars311	Windana (New South Wales,Australia)	-31.27370	149.15670	617	197614	4946	21.86	22.06	0.11	59 ⁺⁴	2019-05-04 2020-08-07
stars314	Dragon's Rest (New South Wales,Australia)	-31.07900	149.37590	540	323160	5404	21.85	22.03	0.11	49 ⁺³	2019-05-05 2020-10-15
stars342	Mudgee Observatory (New South Wales,Australia)	-32.63310	149.49260	607	145635	3701	21.84	22.02	0.11	51 ⁺³	2019-06-05 2020-04-08
stars345	Yuma (New South Wales,Australia)	-30.84220	148.37300	168	226612	5775	21.82	22.04	0.11	60 ⁺³	2019-06-14 2020-10-15
stars274	Old Police Station (South Australia,Australia)	-30.81284	138.41243	241	300219	5815	21.8	22.12	0.13	56 ⁺³	2019-03-26 2020-10-15
stars27	Oukaimeden Observatory (Marrakech-Safi,Morocco)	31.20623	-7.86648	2718	151939	1965	21.79	21.95	0.08	76 ⁺⁴	2018-02-07 2019-12-06
stars213	Obs. Astronómico Nacional (Baja California,Mexico)	31.04350	-115.46410	2797	336241	6525	21.77	22.04	0.11	74 ⁺⁴	2018-10-06 2020-03-27
stars361	Junabee Q. (Victoria,Australia)	-36.80537	144.67604	240	105178	2810	21.76	21.93	0.1	36 ⁺⁴	2020-05-13 2020-10-15
stars62	Centre d'Observació de l'Univers (Catalonia,Spain)	42.02459	0.73480	804	525605	10397	21.76	21.98	0.09	40 ⁺³	2018-02-07 2020-10-15
stars206	Mountain Lodge, Etosha NP (Kunene,Namibia)	-19.25820	15.26240	1186	68105	1321	21.76	21.89	0.09	44 ⁺³	2018-10-09 2019-03-14
stars270	H.E.S.S. (Khomas,Namibia)	-23.27295	16.50283	1817	420186	3361	21.75	21.98	0.11	60 ⁺³	2018-11-29 2020-10-15
stars202	Casa Rural Cijara (Extremadura,Spain)	39.32287	-4.95050	487	230867	6659	21.71	21.95	0.13	60 ⁺³	2018-06-16 2020-07-07
stars230	Long Dark Sky (Wellington,New Zealand)	-41.23592	175.43898	29	401605	5143	21.71	22.06	0.12	34 ⁺³	2018-11-16 2020-10-15
stars18	Javalambre (CEFCA) (Aragon,Spain)	40.04180	-1.01630	1942	248579	6067	21.7	21.93	0.09	38 ⁺³	2018-02-07 2020-08-20
stars219	Hakos Astrofarm (Khomas,Namibia)	-23.23636	16.36177	1824	261055	1876	21.7	21.9	0.09	60 ⁺⁴	2018-10-02 2020-10-15
stars341	Frog Rock (New South Wales,Australia)	-32.45520	149.66290	502	266036	4702	21.66	21.9	0.11	46 ⁺³	2019-06-01 2020-07-24
stars227	Oracle (Arizona,USA)	32.62140	-110.74660	1307	143946	3331	21.65	21.8	0.07	63 ⁺³	2019-03-27 2020-02-10
stars373	Atutahi Observatory (Wellington,New Zealand)	-41.23617	175.48353	72	185930	1687	21.64	21.82	0.1	33 ⁺³	2020-01-04 2020-10-15
stars289	Astrocamp (Castile-La Mancha,Spain)	38.16578	-2.32689	1590	336219	7832	21.61	21.79	0.09	53 ⁺³	2019-03-07 2020-10-15
stars349	Consell Insular de Menorca (Balearic Islands,Spain)	40.04912	4.05414	9	240723	3722	21.6	21.85	0.09	45 ⁺³	2019-07-21 2020-09-13
stars232	Parco Astronomico Lilio (Calabria,Italy)	39.31450	16.75130	1166	422863	7467	21.58	21.8	0.09	48 ⁺³	2018-10-14 2020-10-15
stars66	Hospedería de Monfragüe (Extremadura,Spain)	39.78100	-6.01626	309	435827	9272	21.54	21.78	0.11	68 ⁺⁴	2018-06-16 2020-10-15
stars292	Esparragosa de Lares (Extremadura,Spain)	38.94895	-5.22763	456	213255	5531	21.54	21.88	0.18	52 ⁺³	2019-03-15 2020-09-20
stars221	Complejo Astronómico El Leoncito (SJ,Argentina)	-31.79861	-69.29774	2463	269944	5397	21.52	21.82	0.18	50 ⁺³	2018-11-08 2020-10-15
stars288	Entre Encinas y Estrellas (Extremadura,Spain)	38.21969	-6.63176	493	328279	6930	21.51	21.75	0.11	61 ⁺⁴	2019-01-10 2020-10-15
stars239	Puimichel (Provence-Alpes-Côte d'Azur,France)	43.97808	6.01788	697	152893	4826	21.5	21.69	0.09	60 ⁺³	2018-12-17 2019-12-01
stars220	Pierre Auger Observatory (Mza.,Argentina)	-35.29218	-69.01251	1391	224102	3334	21.49	21.67	0.13	61 ⁺⁴	2019-02-09 2020-07-01
stars296	Casa Rural El Recuerdo (Extremadura,Spain)	39.42861	-5.78417	533	282058	4904	21.45	21.64	0.1	58 ⁺³	2019-05-03 2020-10-15
stars291	Alcazaba de Reina (Extremadura,Spain)	38.18984	-5.95709	813	272833	3936	21.45	21.66	0.08	61 ⁺⁵	2019-03-15 2020-10-15
stars11	El Torcal (Andalusia,Spain)	36.95000	-4.54000	1038	36804	1889	21.4	21.57	0.09	68 ⁺³	2018-02-07 2018-07-05
stars211	OT-IAC (Tenerife,Spain)	28.30033	-16.51221	2384	477139	10824	21.38	21.64	0.12	78 ⁺⁴	2018-02-07 2020-10-15
stars218	La Roca de la Sierra (Extremadura,Spain)	39.10380	-6.66335	258	384440	9884	21.38	21.62	0.09	71 ⁺⁴	2018-10-20 2020-10-15

Table 2 continued

Table 2 (continued)

Name	Place	Latitude (deg)	Longitude (deg)	Alt. (m)	Tot1 (raw)	Tot2 (fil.)	P50	P99	σ	CNT (%)	Dates (yyyy-mm-dd)
stars246	Obs. de Sierra Nevada (Andalusia, Spain)	37.06417	-3.38472	2802	211059	3350	21.38	21.61	0.09	51 ⁺³ ₋₄	2019-06-18 2020-10-15
stars396	Hotel Morvedra Nou (Balearic Islands, Spain)	39.97366	3.90147	79	129536	3318	21.37	21.59	0.09	35 ⁺³ ₋₄	2019-12-17 2020-10-15
stars271	Puerto Villareal (Extremadura, Spain)	38.74252	-7.21002	146	96217	3287	21.34	21.46	0.07	85 ⁺⁴ ₋₆	2018-12-04 2020-10-15
stars242	Joint Ins. for VLBI ERIC (Drenthe, Netherlands)	52.81282	6.39595	16	222049	5404	21.34	21.55	0.11	31 ⁺³ ₋₄	2018-11-14 2020-07-25
stars8	Guirguillano (Navarre, Spain)	42.71167	-1.86509	582	345776	4999	21.25	21.41	0.07	38 ⁺³ ₋₄	2018-02-07 2020-10-15
stars257	Isla Blanca (Balearic Islands, Spain)	39.06986	1.40878	250	158267	2312	21.22	21.34	0.09	53 ⁺³ ₋₅	2019-04-17 2020-07-08
stars201	Finca La Cocola (Extremadura, Spain)	38.75545	-6.98451	244	358402	9260	21.14	21.46	0.16	88 ⁺⁴ ₋₅	2018-06-14 2020-09-19
stars401	Obs. Jost (North Rhine-Westphalia, Germany)	50.52234	6.52818	467	152524	5090	21.14	21.26	0.06	33 ⁺³ ₋₄	2019-12-04 2020-09-14
stars347	Wise Observatory (South District, Israel)	30.59738	34.76226	863	261080	4961	21.07	21.33	0.13	90 ⁺⁶ ₋₆	2019-08-21 2020-10-15

NOTE—A total of 44 TESS devices are included in the present work comprising a raw data total of 11,099,432 individual measurements. After filtering (see Section 3) the total number of clear data is reduced to 222,605. All the photometers are still collecting data, but the present analysis is limited to the end date 2020 October 15. Exact dates are shown in the last column (Dates). P50 and P99 are the m_{TESS} in units of magnitude per square arcsecond. The values of σ are the standard deviations of the magnitude distributions. The CNT column is an estimation of the percentage of clear night time on every photometer by means of the ROC curve method explained in Section 3.1.

APPENDIX

A. TESS PHOTOMETRIC ERRORS

Following standard astronomical practice, brightness is usually expressed in units of magnitude per square second. For the TESS photometric band it is defined as (Bará et al. 2019):

$$m_{\text{TESS}} = ZP - 2.5 \log_{10}(f_{\text{TESS}} - f_{\text{TESS}}^{\text{D}}) \quad (\text{A1})$$

where ZP is the laboratory-defined zero-point of the photometer using a reference light source and an absolute-calibrated sensor inside an integrating sphere, and f_{TESS} and $f_{\text{TESS}}^{\text{D}}$ are the signal and dark frequencies of the sensor, respectively, both measured in hertz. At typical nighttime low operating temperatures ($< 20^\circ$), the value of $f_{\text{TESS}}^{\text{D}}$ turns out to be negligible in most cases. The total uncertainty (uncertainty and error are used indistinctly in this section), $\delta^2 m_{\text{TESS}}$, of the measurements of the TESS photometer for the output frequency f_{TESS} is obtained and converted to device-specific brightness units by propagating expression (A1) as follows,

$$\delta^2 m_{\text{TESS}} = \delta_{ZP}^2 + \left(\frac{2.5 \log_{10}(e)}{f_{\text{TESS}}} \delta_{f_{\text{TESS}}} \right)^2 = \text{Calibration Error}^2 + \text{Instrumental Error}^2 \quad (\text{A2})$$

Considering a calibration and instrumental error of 0.044 and 0.002 mag/arcsec², respectively (see next sections for details), the final calculated error will be equal to 0.04404 mag/arcsec². An uncertainty of 0.04 mag/arcsec² is adopted for the magnitudes measured by the TESS photometers. A measurement intercomparison of several TESS photometers at the same site in dark-sky conditions is done to validate this value. Figure 15 shows the distribution of the difference in zenithal NSB measurements between three TESS photometers—stars426, stars427, and stars211—placed adjacent to one another at OT during a period of 2 months (2020 June and July). The NSB statistical percentiles of the TESS photometers are shown in Table 3. In both percentile cases, the final adopted magnitude uncertainty is in good agreement with the experimental data.

To study the nighttime evolution of NSB and possible correlations with different atmospheric and astronomical sources, differential photometry must be done to measure magnitudes from two different TESS photometers. Considering two photometer measurements taken at the same time t , and neglecting dark currents, magnitudes are defined following Equation (A1) as

$$\begin{aligned} m_{\text{TESS1}}(t) &= ZP1 - 2.5 \log_{10}(f_{\text{TESS1}}(t)) \\ m_{\text{TESS2}}(t) &= ZP2 - 2.5 \log_{10}(f_{\text{TESS2}}(t)) \end{aligned} \quad (\text{A3})$$

and the result of differential photometry is

$$\Delta m_{\text{TESS}}(t) = m_{\text{TESS2}}(t) - m_{\text{TESS1}}(t) = 2.5 \log_{10} \left(\frac{f_{\text{TESS1}}(t)}{f_{\text{TESS2}}(t)} \right) + (ZP2 - ZP1) \quad (\text{A4})$$

Assuming $ZP1$ and $ZP2$ are constants (calibration error is considered to be a systematic error), the total squared uncertainty for differential photometry, $\delta^2 \Delta m_{\text{TESS}}$, is obtained and converted to device-specific brightness units by propagating the previous expression:

$$\delta^2 \Delta m_{\text{TESS}} = (2.5 \log_{10}(e))^2 \left(\left(\frac{\delta_{f_{\text{TESS1}}(t)}}{f_{\text{TESS1}}(t)} \right)^2 + \left(\frac{\delta_{f_{\text{TESS2}}(t)}}{f_{\text{TESS2}}(t)} \right)^2 \right) \quad (\text{A5})$$

Working with a NSB around 21 mag/arcsec², $f_{\text{TESS1}}(t) \approx f_{\text{TESS2}}(t) = f_{(m_{\text{TESS}}=21)} = 0.592$ Hz, therefore $\delta_{f_{\text{TESS1}}(t)} \approx \delta_{f_{\text{TESS2}}(t)} = \delta_{f_{(m_{\text{TESS}}=21)}} = 0.0009$ mag/arcsec² (see Figure 14) and final differential photometry error will be

$$\delta \Delta m_{\text{TESS}} = \left(\frac{(2.5 \log_{10}(e))\sqrt{2}}{f_{(m_{\text{TESS}}=21)}} \right) \delta_{f_{(m_{\text{TESS}}=21)}} = 0.0023 \text{ mag/arcsec}^2 \quad (\text{A6})$$

This result (that is, the analog for $m_{\text{TESS}} = 22$ mag/arcsec²) should be considered theoretical. When differential photometry is applied to real data, the photometric uncertainty is around 0.02 mag/arcsec², as shown in Figure 15 (standard deviation). This error increase is caused by unknown and unpredictable small changes in the environmental conditions and photometer internal conditions.

Table 3. Percentile 50 and 99 of Zenithal NSB for Three Identical TESS Photometers Installed Adjacent to One Another at OT.

Name	P50 (OT)	P99 (OT)	Total
	(mag/arcsec ²)	(mag/arcsec ²)	raw (filtered)
stars426	21.26 ± 0.04	21.41 ± 0.04	32,148 (300)
stars427	21.28 ± 0.04	21.43 ± 0.04	22,350 (342)
stars211	21.24 ± 0.04	21.39 ± 0.04	32,903 (300)

NOTE—Data were taken during 2020 June and July. Only filtered data (see Section 3 for details) have been used to calculate the percentiles.

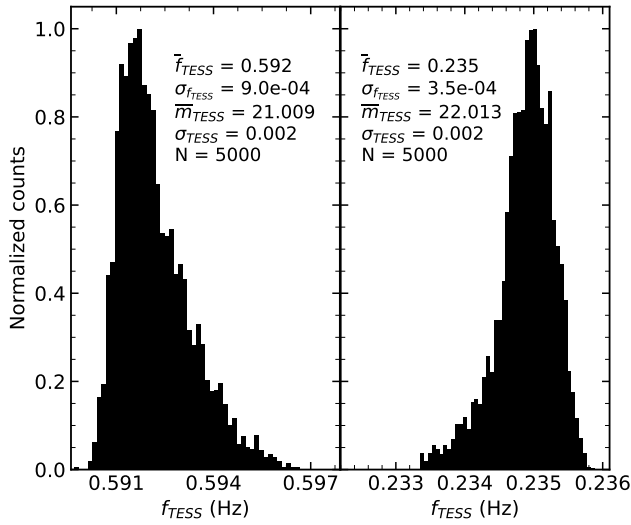


Figure 14. Distribution of 5000 laboratory measurements with light intensities equivalent to $m_{\text{TESS}} = 21$ (left) and 22 (right) mag/arcsec². The standard deviation of the distribution, in both cases $\sigma_{\text{TESS}} = 0.002$, is considered an upper bound on the instrumental error.

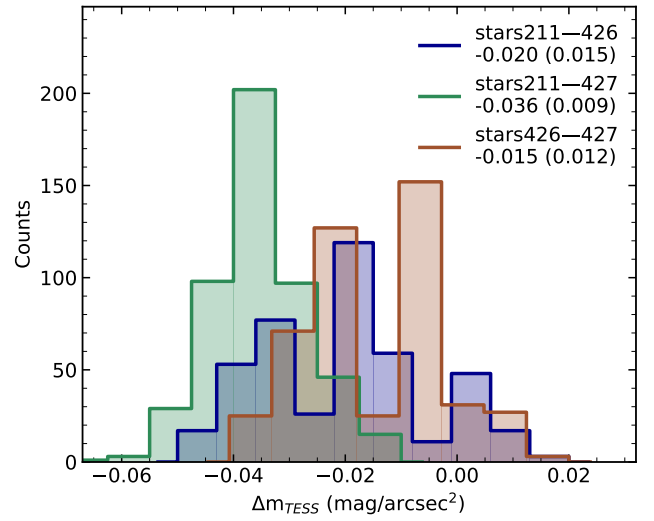


Figure 15. Measurement intercomparison between three TESS photometers— stars426, stars427, and stars211—placed adjacent to one another at OT. The histograms show the distribution of the difference in zenithal NSB measurements. In total, about 300 measurements have been compared, whose mean difference and (standard deviation) are shown in the plot.

A.1. TESS Calibration Error

The TESS devices are calibrated by the manufacturer in the Laboratory for Scientific Advanced Instrumentation (Laboratorio de Instrumentación Científica Avanzada) of UCM (Spain) using a photodiode and a TESS photometer unit, both calibrated absolutely (see Bará et al. (2019) for the absolute calibration procedure). For the first 39 TESS photometers manufactured, the mean value of the measured zero-points was $ZP = 20.44$ mag/arcsec² showing a dispersion of $\sigma = 0.044$ mag/arcsec² (see Figure 5 of Zamorano et al. (2017b)). This well-defined calibration method for the TESS photometer allows for intercomparison among the measurements of several TESS devices of different research teams.

A.2. TESS Instrumental Error

The sky brightness detector is a TSL237 photodiode that converts light to frequency. It is the same sensor used by the SQM photometer (Cinzano 2007). However, the bandpass of TESS is more extended to the red range because of the use of a dichroic filter. Figure 16 shows a comparison of the spectral responses of the SQM and TESS photometers (Johnson–Cousins filters are also included). A typical night sky spectrum is also shown.

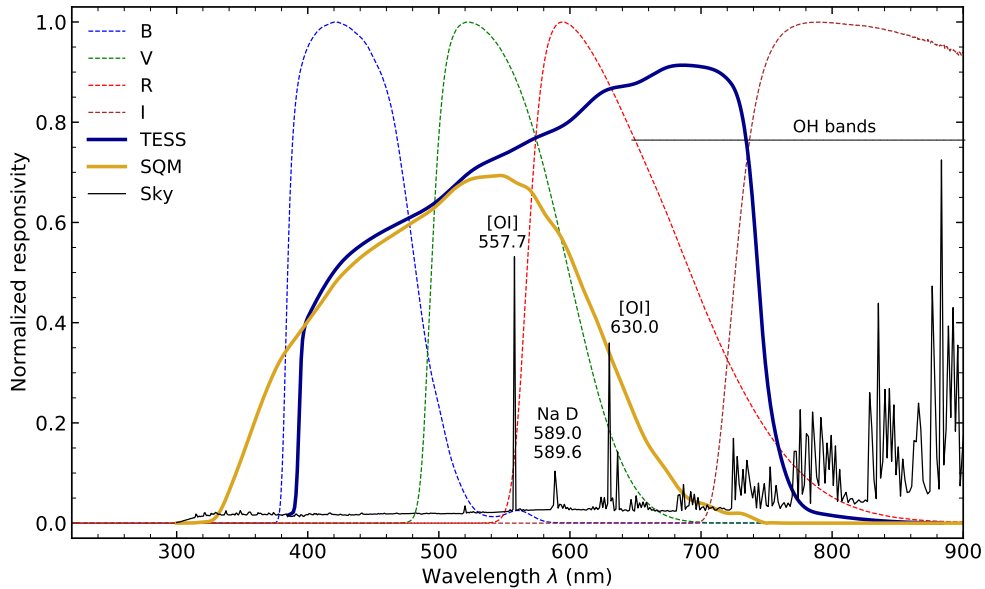


Figure 16. Spectral response curve of the TESS photometer. The sensitivity of the TSL237 sensor is limited to the visible range by a dichroic filter, which reaches redder wavelengths than the SQM. The transmissivity of the Johnson–Cousins (Bessell 1990) filters has been included for reference, as well as the night sky spectrum obtained using the SkyCalc tool (Noll et al. 2012), where the brightest airglow lines are labeled.

The stability of the measurements was studied in order to characterize the intrinsic error of the optical system. To do so, 5000 measurements were performed for TESS magnitudes of 21 and 22 mag/arcsec² (the NSB values expected for the dark sites included in this work). For each set of 5000 measurements, a histogram of frequency was obtained (represented in Figure 14), along with its mean and standard deviation. The final adopted instrumental error is 0.002 mag/arcsec² for both magnitudes. This is an upper limit, because of the nonzero possibility that it may include the power supply or lamp variability, external diffuse light, or even electromagnetic interference. The measurements presented here have been made in collaboration with Sieltec Canarias S.L. The power source employed was a PS 2042-20B (Elektro-Automatik), with a HALOSTAR 50 W 12 V GY6.35 (OSRAM) lamp and an AvaSpec-ULS3648-UA-25 (AVANTES) spectrometer with a resolution of 1.1 nm.

Figure 9 shows the distribution of the standard deviation grouping the data of each photometer at different time intervals, from minutes to months. On the minute timescale, the calculated σ_{TESS} is below 0.004 mag/arcsec², compatible with the instrumental error obtained above.